



Contents lists available at ScienceDirect

Arabian Journal of Chemistry

journal homepage: www.ksu.edu.sa

Experimental and theoretical study on corrosion inhibition and adsorption performance of *Ipomoea batatas L.* leaf extract for mild steel

Bi-lan Lin^{a,*}, Xin-xin Zhou^a, Tian-hu Duan^a, Chen Zhao^a, Jia-hao Zhu^a, Yu-ye Xu^{b,*}

^a School of Material Science and Engineering, Xiamen University of Technology, No.600 Ligong Road, Jimei District, Xiamen, Fujian Province, China

^b College of Civil Engineering, Huaqiao University, No.668 Jimei Avenue, Jimei District, Xiamen, Fujian Province, China

ARTICLE INFO

Keywords:

Mild steel
Ipomoea batatas L. leaf
 Plant extract
 Corrosion inhibitor
 Molecular dynamics
 Adsorption

ABSTRACT

Recent years have seen a surge in interest in efficient, green, and eco-friendly corrosion inhibitors, leading to extensive research on plant extracts. This study investigates the active phytochemicals in abundant *Ipomoea batatas L.* leaves, which were extracted with ultrasonics using an ethanol–water solution and applied to mitigate the corrosion of mild steel (MS) in a 1 M HCl pickling solution. The chemical compositions and corrosion inhibition properties of the leaf extract of *Ipomoea batatas L.* (IBLE) were explored through multiple experiments, and the adsorption thermodynamic and kinetic parameters were analysed. Electrochemical results indicated that the corrosion inhibition mechanism of IBLE is a geometric coverage effect; IBLE acts as a mixed-corrosion inhibitor; and the inhibition efficiency increases with extract concentration and solution temperature, reaching up to 96.4 % at 318 K. X-ray photoelectron spectroscopy (XPS) results showed the adsorption of C=C, C–N, C–N⁺, C=N, C=N⁺, C=O, C=O⁺, C–O, C–O⁺, Fe–N and other carbonaceous groups on the steel surface. Surface observation confirmed that IBLE can effectively retard steel corrosion. The adsorption analysis revealed that the protective film is a monolayer that follows the Langmuir isotherm, and the oriented adsorption of active ingredients enhances the order of the MS surface. Density functional theory (DFT) and molecular dynamics (MD) simulations were conducted to examine the relationship between inhibition and adsorption of IBLE. The theoretical calculations confirmed that the active compounds in IBLE can adsorb on the Fe (110) surface through physical patterns and by sharing charges with iron to form coordinate bonds. The adsorption abilities of different ingredients vary, but all exhibit synergistic adsorption effects. IBLE can be considered an efficient and renewable corrosion inhibitor for MS in HCl pickling media.

1. Introduction

Mild steel (MS) is widely used in various industries such as machinery, automobiles, aerospace, petroleum, chemical engineering, and construction due to its straightforward processing, affordability, and excellent mechanical properties. However, its poor corrosion resistance has raised significant concerns (Bahlakeh et al., 2019; Singh et al., 2015; Zhu et al., 2021). The two most common and effective protection methods are applying a covering layer and using a corrosion inhibitor (Radwan et al., 2021). Pickling is an essential pre-treatment process for applying a protective layer. Commonly used acids for this process include hydrochloric acid, sulfuric acid, and their mixtures, as well as nitric acid, hydrofluoric acid, phosphoric acid, and some organic acids. Hydrochloric acid is frequently used due to its low tendency for

hydrogen permeation, rapid rust and scale removal speed, no heating requirement, and energy-saving properties. While pickling removes rust and scale, it also corrodes metal substrates and produces acid mist. Therefore, efficient corrosion inhibitors must be added to the pickling solution (Rezaeiava et al., 2022; Wazzan, 2023). However, most available inhibitors are expensive, toxic, non-biodegradable, and produce many by-products that contaminate the environment.

Similar to the synthetic organic corrosion inhibitors (Dewangan et al., 2022; Verma et al., 2021), there are many adsorptive functional groups, such as aromatic rings, heterocycles containing N, O, S, or P, unsaturated bonds, carbonyls, and hydroxyls, in the active components of plant extracts. Currently, plant extracts have been used as green, economical, and effective corrosion inhibitors in mild steels (Chen et al., 2023; Karki et al., 2021), stainless steels (Bhardwaj et al., 2021 and

Peer review under responsibility of King Saud University.

* Corresponding authors.

E-mail addresses: linbilan@xmut.edu.cn (B.-l. Lin), yuyexu@hqu.edu.cn (Y.-y. Xu).

<https://doi.org/10.1016/j.arabjc.2023.105410>

Received 24 June 2023; Accepted 29 October 2023

Available online 31 October 2023

1878-5352/© 2023 The Authors. Published by Elsevier B.V. on behalf of King Saud University. This is an open access article under the CC BY-NC-ND license (<http://creativecommons.org/licenses/by-nc-nd/4.0/>).

2022), pipeline steels (Kalyn et al., 2022), aluminium alloys (Fernine et al., 2021; Khadraoui et al., 2016), copper alloys (El-Asri et al., 2022; Kusumaningrum et al., 2022), and other metals. The raw sources of plants mainly include leaves, fruits, peels, flowers, and stems, such as mangrove leaf (Alsalhi et al., 2023), olive leaf (Philippe et al., 2020), *Ruellia tuberosa* L. leaf (Kathiravan et al., 2021), *Azadirachta indica* leaf (Swaroop et al., 2016), *Citrullus lanatus* fruit (Dehghani et al., 2019a), *Gardenia jasminoides* fruit (Xu et al., 2022), *Garlic* (Pereira et al., 2012), *Garcinia indica* (Thomas et al., 2020), *Apricot* pomace (Vorobyova et al., 2022), *Pomelo* peel (Lin et al., 2021), *Longan* seed and peel (Liao et al., 2017), *Passiflora edulis* Sims peel (Lin et al., 2023), *Borage* flower (Dehghani et al., 2019b), *Cordia dichotoma* (Sharma and Sharmab, 2019), *Biebersteinia multifida* root (Khayatkashani et al., 2022). *Cinnamomum Tamala* leaf extract was prepared via Soxhlet extraction and used as a corrosion inhibitor for MS in a 0.5 M H₂SO₄ solution (Prasad et al., 2022). Electrochemical results showed that the corrosion mechanism of MS did not vary, and the inhibition efficiency was 96.7 % with 0.1 mg/L extract. DFT simulations confirmed the interactions between the benzene rings, heterocycles, and Fe atoms (Prasad et al., 2022). *Artemisia argyi* leaf extract (ALE) acted as a mixed corrosion inhibitor for carbon steel in 1 M HCl solution, and the inhibition efficiency increased with extract concentration but decreased with solution temperature (Wang et al., 2022). The electrostatic diagram showed that the active sites in the ALE molecules were mainly distributed near the oxygen atoms (Wang et al., 2022). *Triticum aestivum* extract was used as a corrosion inhibitor for stainless steel in a 15 % HCl solution. The adsorption of the extract obeyed the Langmuir isotherm and was physically adsorbed with an inhibition efficiency of 92.7 % (Bhardwaj et al., 2021). *Punica granatum* peel extract (PGPE) acted as an anodic inhibitor for stainless steel in a 15 % HCl solution, and the inhibition efficiency was 97.8 % with 4.0 g/L extract (Bhardwaj et al., 2022). Theoretical calculations demonstrated that the molecules in the extract could donate electrons to the empty 3d orbital of Fe (Bhardwaj et al., 2022). However, PGPE was a mixed inhibitor for copper in an HNO₃ solution, and the inhibition efficiency with 0.8 g/L extract at 298 K was 98.5 % (Kusumaningrum et al., 2022). The extract contained many antioxidant groups, and the adsorption complied with the Frumkin isotherm (Kusumaningrum et al., 2022). Plant extracts, rich in active ingredients, can be obtained easily. Recently, extensive research has been carried out the use of plant extracts as inhibitors of metal corrosion. However, a rich plant source is crucial for its promotion as a corrosion inhibitor.

Ipomoea batatas L. leaves, also known as sweet potato leaves, comprise tender leaves and stems. Both *Ipomoea batatas* L. and its leaves are edible. Owing to their high yield, favourable growing conditions, and rich nutritional content, *Ipomoea batatas* L. has been extensively cultivated worldwide. An ethanol extract of *Ipomoea batatas* L. leaf was prepared through refluxing, filtration, and concentration; D-xylose, D-mannose, D-glucose, quercetin, coumarin, and ethyl caffeate were identified (Zhang et al., 2007). Ethyl acetate, acetone, and ethanol were respectively employed as extraction solvents for *Ipomoea batatas* L. leaves, and in ethanol extract, the additional organic substances such as ethyl caffeate, quercetin, rutin, kaempferol, luteolin, and catechin hydrate were detected (Luo et al., 2021). Liquid chromatography-mass spectrometry revealed that *Ipomoea batatas* L. leaf extract (IBLE) contained xanthoside, vitamin B₂, nicotinic acid, carotene, vitamin C, chrysin, protocatechualdehyde, and other compounds (Rodriguez-Perez et al., 2018). D-xylose, D-mannose, D-glucose, and xanthine are sugars; vitamins B₂, nicotinic acid, carotene, and vitamin C are vitamins; coumarins, quercetin, rutin, and chrysin are flavonoids; protocatechualdehyde and ethyl caffeate are phenolic acids. IBLE possesses numerous polar functional groups, such as aromatic rings, hetero-atoms, double bonds, carbonyl, hydroxy, and ketone. Coordination bonds may form through electron sharing with metal atoms, and electrostatic attraction with the charged metal surface may also be generated. These components may adsorb on the metal surface via chemical, physical, or mixed adsorption, forming a corrosion barrier film and inhibiting metal

corrosion. Currently, research on IBLE as green corrosion inhibitor for metals is rare (Zeng et al., 2021). Nevertheless, due to the abundant raw materials, the investigation of the corrosion inhibition and adsorption properties of IBLE is still of great significance.

In this study, we explored the use of IBLE as a sustainable corrosion inhibitor for mild steel (MS) in a 1 M HCl pickling solution at various temperatures. The inhibition behaviours and chemical compositions of IBLE were characterised through multiple tests and adsorption isotherms, and the thermodynamic and kinetic parameters of adsorption were examined. We conducted DFT and MD simulations to further investigate the adsorption capacity and behaviours of the active phytochemicals in IBLE on the surface of MS. As depicted in Fig. 1, D-mannose, vitamin B₂, quercetin, and protocatechualdehyde were selected as representatives of sugars, vitamins, flavonoids, and phenolic acids, respectively, to display their simulation results. Finally, we discussed the adsorption and corrosion inhibition mechanism of IBLE.

2. Materials and methods

2.1. Extraction of IBLE

Fresh leaves of *Ipomoea batatas* L. were cleaned, air-dried, and then oven-dried at 80 °C until they reached a constant weight. The dried leaves were ground into a powder, and coarse particles were removed using a 100-mesh sieve. An extraction solvent of 200 mL (ethanol: water = 4:1 v/v%) was prepared, into which an appropriate amount of the powdered leaves was added. After thorough stirring, the mixture underwent ultrasonic vibration at 40 °C for 4 hours to ensure the dissolution of the active ingredients. The filtered extraction solution was then concentrated using a rotary evaporator. Finally, the super-concentrated solution was thoroughly dried in an oven at 80 °C until it reached a constant weight. The end product was a solid dark-green substance referred to as IBLE. Notably, the ethanol used in this process can be recycled and reused, and no by-products were generated throughout the entire process.

2.2. Materials and corrosion media

The tested materials were MS with a dimension of 1.0 cm × 1.0 cm × 0.2 cm. The chemical compositions were as follows (wt. %): 0.38 Mn, 0.2Si, 0.13C, 0.014P, 0.031 S, and balance Fe.

The corrosion medium was 1 M HCl solution prepared by diluting hydrochloric acid (36.5 %) with distilled water. The concentrations of IBLE added were 0.1, 0.5, 1.0, 3.0, and 5.0 g/L, respectively. A 1 M HCl solution without IBLE was denoted as the blank solution. The temperatures of the corrosion media were controlled using electronic thermostats at 298, 308, and 318 K, respectively.

2.3. Preparation of the working electrode

A 1.0 cm × 1.0 cm face of the tested sample was selected as the working surface. A copper wire was welded to the reverse side and wrapped with three layers of heat-shrinkable tubes for insulation. Except for the working surface, all parts of the sample, including the welded points, were sealed with epoxy resin. The unnecessary galvanic corrosion effects were avoided. The working surface was step by step polished with waterproof sandpaper (No. 400 – No. 2000), followed by scrubbing with ethanol, rinsing with distilled water, and drying with cold air. The working electrode was acquired for electrochemical measurements.

2.4. Electrochemical tests

Electrochemical measurements, including open-circuit potential (OCP), electrochemical impedance spectroscopy (EIS), and potentiodynamic polarization (PDP), were performed using a Corrtest instrument

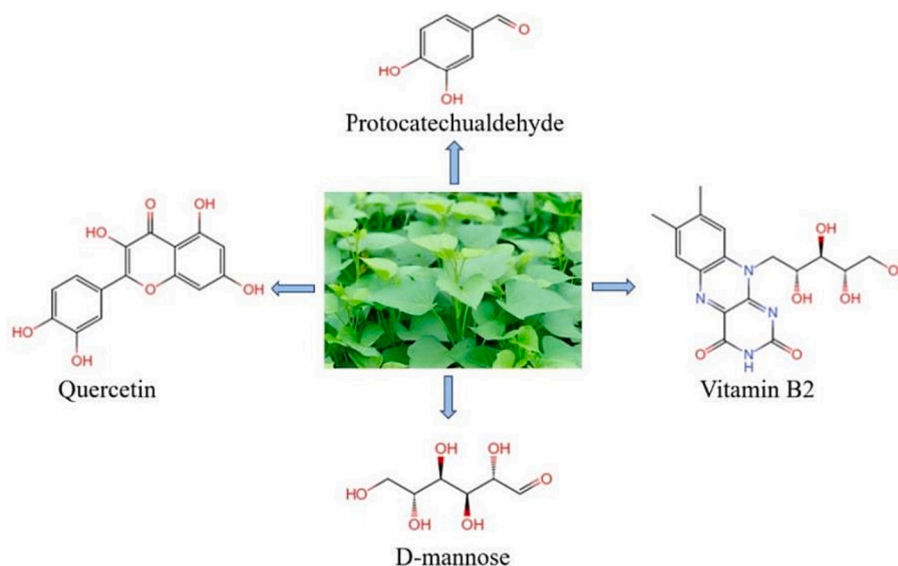


Fig. 1. Chemical structures of four typical components in IBLE used to display the results of theoretical calculations.

(CS310H, Wuhan Corrtest Instrument Corp., Ltd., China). A traditional three-electrode system was established. The working electrode was the tested MS sample prepared as described above; the auxiliary electrode was a platinum electrode, and the reference electrode was a saturated calomel electrode (SCE).

Because the EIS and PDP tests must be based on a nearly stable state, the OCP of the corrosion system must be first monitored to ascertain the dynamic equilibrium. Furthermore, the OCP monitoring time for each process was one hour.

The EIS test is a nearly non-destructive technique that can provide a wealth of information about the interface between metal and solution, including charge-transfer resistance and electric double-layer capacitance. The EIS tests were performed immediately after the OCP test. The initial potential corresponded to the above stable OCP. The frequency range was $10^5 \sim 10^2$ Hz. The AC signal amplitude was 10 mV. The Zview software was used to fit the EIS data.

To establish the Tafel segments of the cathode and anode, the polarization potential of the PDP test ranged from -300 to 300 mV vs. OCP. The Tafel test is a strong-polarization technique in which the working electrode is severely damaged. The PDP test was conducted immediately after the EIS test. The common scan rate of the corrosion system, 1 mV/s, was set. Polarization parameters such as the corrosion potential (E_{cor}), corrosion current density (i_{cor}), anodic Tafel slope (b_a), and cathodic Tafel slope (b_c) were obtained by Tafel extrapolation. The corrosion protection efficiency of IBLE for MS in 1 M HCl solution, denoted by η_{PDP} , was calculated using the following expression (Aljourani et al., 2009; Hemapriya et al., 2020):

$$\eta_{PP} = (1 - i_{cor}/i_{cor,0}) \times 100\% \quad (1)$$

where $i_{cor,0}$ and i_{cor} are the corrosion current densities of MS in 1 M HCl solution with and without IBLE, respectively.

2.5. Fourier transform infrared spectrophotometers (FTIR) analysis

The transmittance of the thoroughly dried IBLE was recorded using an FTIR spectrometer (ALPHA, Bruker, Germany). The wavenumber ranged from 4000 to 400 cm^{-1} . The stretching and bending vibrations of various bonds in the active ingredients were analysed to determine the presence of the adsorptive functional groups.

2.6. UV-visible spectroscopy analysis

A 50 mL corrosion solution containing 1 M HCl and 5.0 g/L IBLE was divided into two parts. A polished and thoroughly cleaned MS sample was submerged in one part for 24 hours, and this solution was denoted as "after immersion". The other part was marked as "before immersion". The absorbances of two solutions were recorded using an UV-visible spectrophotometer (UV-2700, Shimadzu, Japan). The wavelength range was from 200 to 800 nm. The scanning interval was 1 nm. Distilled water was used as the reference solution.

2.7. X-ray photoelectron spectroscopy (XPS) analysis

A polished and cleaned MS specimen was immersed in a 1 M HCl solution containing 5.0 g/L IBLE for 3 hours. Upon removal, the sample was immediately rinsed with distilled water, gently scrubbed with cotton swabs, and dried in cool air. An adsorption film of the active ingredients in IBLE was formed on the MS surface. The specimen was characterised using the XPS technique (AXIS SUPRA+, Shimadzu, Japan). The binding energy (BE) of a monochromatic Al-K α X-ray source was 1486.6 eV, and the C $1s$ peak with BE of 284.8 eV was used for correction. The full spectrum of the adsorbed film was initially recorded, and subsequently, high-resolution spectra of C $1s$, N $1s$, O $1s$, and Fe $2p_{3/2}$ were obtained. The forms of these elements were analysed using XPSPEAK41 software.

2.8. Surface observation

To assess the impact of IBLE on the surface morphology of the corroded MS, three polished and cleaned steel samples were immersed in 1 M HCl solutions. These solutions were without IBLE and with 1.0 and 5.0 g/L IBLE, respectively. The corrosion time was set to 3 hours. The subsequent cleaning process was similar to that described in the XPS analysis. The surface observation was done using a Scanning Electron Microscope (SEM, Evo 18, Zeiss, Germany).

3. Theoretical calculations

3.1. Density functional theory (DFT) simulations

Quantum chemical calculations of the active components in IBLE were conducted using Gaussian 09 W software. DFT simulations were

performed with the 6-31G**(d, p) basis set of the B3LYP function (Berdimurodov et al., 2021; Khadom et al., 2021). Initially, the geometric equilibrium configurations of the active components in a neutral state were established. In acidic media, the hetero-atoms in organic molecules may be protonated with hydrogen ions to form onium ions, which carry a positive charge. However, the equilibrium configuration will be affected when the protonated atoms differ. The geometric configuration for each hetero-atom in protonation was calculated. The most favourable atom for protonation was identified, and the corresponding equilibrium geometry in the protonated state was constructed, as illustrated in Fig. 2. Furthermore, the distributions of the frontier molecular orbitals, namely the highest occupied molecular orbital (HOMO) and the lowest unoccupied molecular orbital (LUMO), were calculated to evaluate the electron donation and/or acceptance trends. The reaction activity parameters were determined to investigate electron stability, adsorption ability, and corrosion inhibition effects.

3.2. Molecular dynamics (MD) simulations

To examine the adsorption patterns and stability of the active components on the MS surface, MD simulations were conducted using the Forcite module in Materials Studio 8.0 (MS) software. The Fe (110) plane, which has the lowest thermodynamic energy, was used to analyse the adsorption behaviour (Nikpour et al., 2019). The cell size was set to 2.48 nm × 2.48 nm × 6.22 nm, with a vacuum layer thickness of 30 Å, comprising one organic molecule and 500 water molecules. The force field was COMPASS (Alibakhshi et al., 2018), and the thermostat was controlled by Andersen. The ensemble was NVT (Zhang et al., 2021).

4. Results and discussion

4.1. Chemical compositions

4.1.1. FTIR analysis of IBLE

The FTIR spectrum of IBLE is shown in Fig. 3. The absorption band at 3204 cm⁻¹ corresponds to the stretching vibrations of the hydroxyl and amino groups (Hu et al., 2020). The absorption band at 2937 cm⁻¹ is attributed to the stretching vibration of the saturated carbon-hydrogen bond (Chen et al., 2020). The adsorption band at 1609 cm⁻¹ is responsible for the stretching vibration of C=C in aromatic rings (Shahmoradi et al., 2021; Wan et al., 2022). The absorption band at 1510 cm⁻¹ is due to the stretching vibrations of C-C in aromatic rings and C=O in flavonoids (Bhardwaj et al., 2022). The absorption bands at 1344 and 1385 cm⁻¹ correlate with the bending vibration of the methyl group (Wan et al., 2022). The absorption band at 1046 cm⁻¹ corresponds to the stretching vibration of C-O in aromatic rings (Wang et al., 2022). The absorption band at 1006 cm⁻¹ can be attributed to the stretching vibration of C-O in fatty ether (Bhardwaj et al., 2022). The absorption bands below 1000 cm⁻¹ can be ascribed to the bending vibration of C-H in benzene rings and/or heteroaromatic rings (Lin et al., 2021). Therefore, functional groups such as -OH, -NH, C=C, C=O, C-O, C-C, and -CH₂ (or -CH₃, -CH), which may be due to D-mannose, vitamin B2, quercetin, and protocatechualdehyde, were detected in the

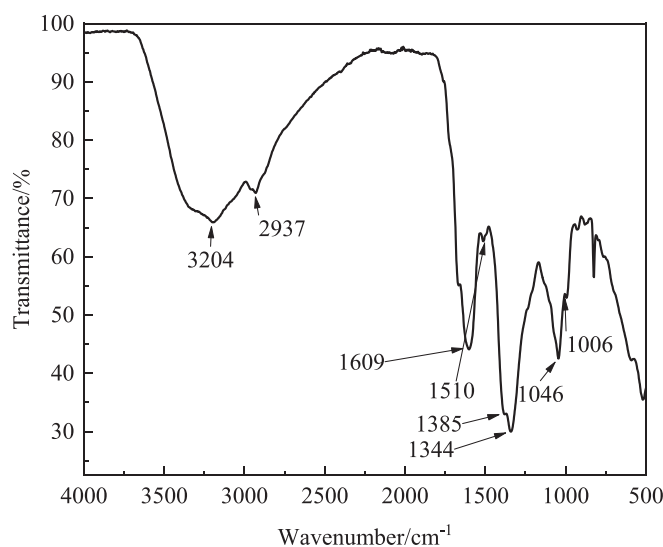


Fig. 3. FTIR spectrum of IBLE.

IBLE. Aromatic and/or heteroaromatic rings were also observed. The polar groups, aromatic rings, and heterocyclic rings possess specific electronic structures that can share electrons with iron atoms, adsorbing on the metal surface.

4.1.2. UV-visible spectra of the corrosion media

The UV-visible spectra of the corrosion media, i.e., a 1.0 M HCl solution containing 5.0 g/L IBLE before and after the immersion of the MS sample are depicted in Fig. 4. Before the corrosion of MS, the first strong absorption peak appearing at 268 nm corresponds to the π - π^* transition of C=O in carbonyl compounds (Fernandes et al., 2019). The second broad absorption band at 333 nm can be attributed to the n - π^* transition of O-H (Asfia and Rezaei, 2021). The peak intensity decreased when the MS sample was submerged, and the peak position slightly red-shifted. The first absorption peak shifted to 273 nm, while the second peak almost disappeared. This phenomenon can be attributed to the interaction of C=O and O-H in the active ingredients of IBLE with Fe atoms/ions (Mostafatabar et al., 2022; Sigircik et al., 2017; Tehrani et al., 2021). It suggests that the active compounds in IBLE can interact with iron and thus adsorb onto the surface of MS.

4.1.3. XPS analysis of the adsorption film

To further understand whether the active ingredients were adsorbed onto the MS surface, the XPS technique was used to analyse the elemental compositions of the corrosion product film, i.e. the adsorption film. After peak fitting, BE deduced the valence states and existing forms of the elements, and the relative atomic content was evaluated based on the peak area. The high-resolution XPS spectra of C 1s, N 1s, O 1s, and Fe 2p_{3/2} in the IBLE adsorption film on the MS surface are shown in Fig. 5.

As shown in Fig. 5a, the C 1s spectrum consists of three peaks with BE

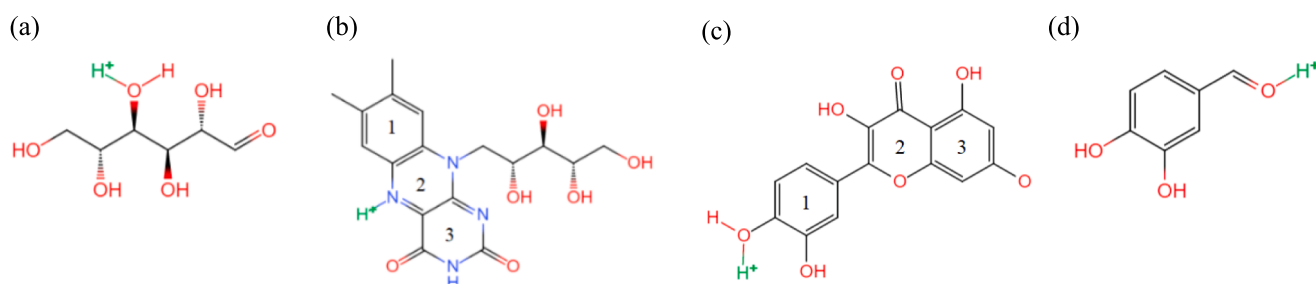


Fig. 2. Protonated form of (a) D-mannose, (b) Vitamin B2, (c) Quercetin, and (d) Protocatechualdehyde in IBLE.

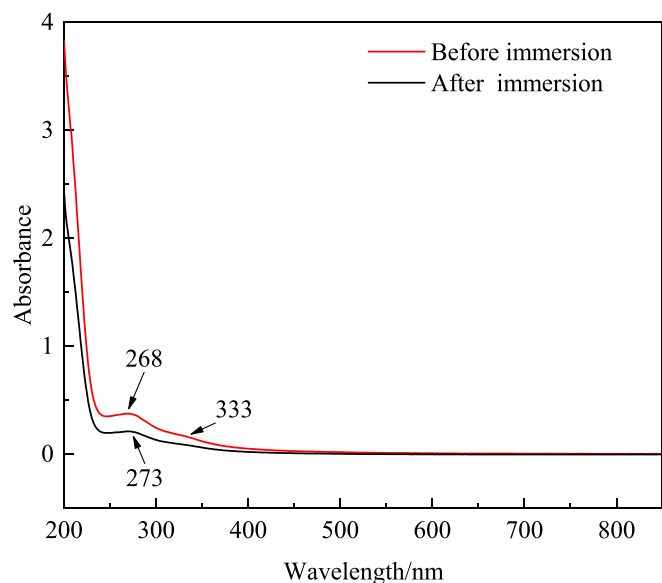


Fig. 4. UV-visible spectra of a 1 M HCl solution containing 5.0 g/L IBLE before and after immersion of MS sample.

values of 284.8, 285.7, and 288.6 eV, respectively. The first strong peak at 284.8 eV corresponds to C 1s in C–C, C–H, and C=C in aromatic rings (Azzouzi et al., 2022), which may originate from vitamin B2, quercetin, protocatechualdehyde, and other components in IBLE. The second peak at 285.7 eV corresponds to C 1s in C=O, C–O, C=O⁺, and C–O⁺ (Ahmed and Zhang, 2020), which may stem from D-mannose, vitamin B2, quercetin, protocatechualdehyde, etc. The third minor peak at 288.6 eV is related to C–N, C–N⁺, C=N, and C=N⁺ (Bouanis et al., 2016; Dehghani et al., 2019a), possibly due to vitamin B2 or other amino acids. The high-resolution XPS spectrum of C 1s indicates that the active components in IBLE participate in adsorption to form a protecting film.

As shown in Fig. 5b, the N element exists in two ways. The peak at 399.7 eV corresponds to C–N, C–N⁺, C=N, and C=N⁺ (Olivares-Xometl et al., 2006; Xu et al., 2022), possibly due to the N 1s in the heterocycles of vitamin B2. The peak at 400.3 eV can be attributed to N–Fe bonds in the heterocycles of vitamin B2, which can share electrons with the unfilled and filled 3d orbitals of the iron atoms. Chelates are formed between vitamin B2 and iron via N–Fe bonds. Thus, vitamin B2 was adsorbed onto the MS surface to inhibit corrosion.

As shown in Fig. 5c, the O 1s peak in the adsorbed film comprises three types of compounds. The peak at 529.9 eV is attributed to the O 1s in iron oxides Fe₂O₃ and Fe₃O₄ (Mukhopadhyay et al., 2021). The peak at 531.9 eV corresponds to the O 1s in FeOOH (Hu et al., 2021). The peak at 533.7 eV might be connected to the O 1s in C=O, C–O, C=O⁺, and

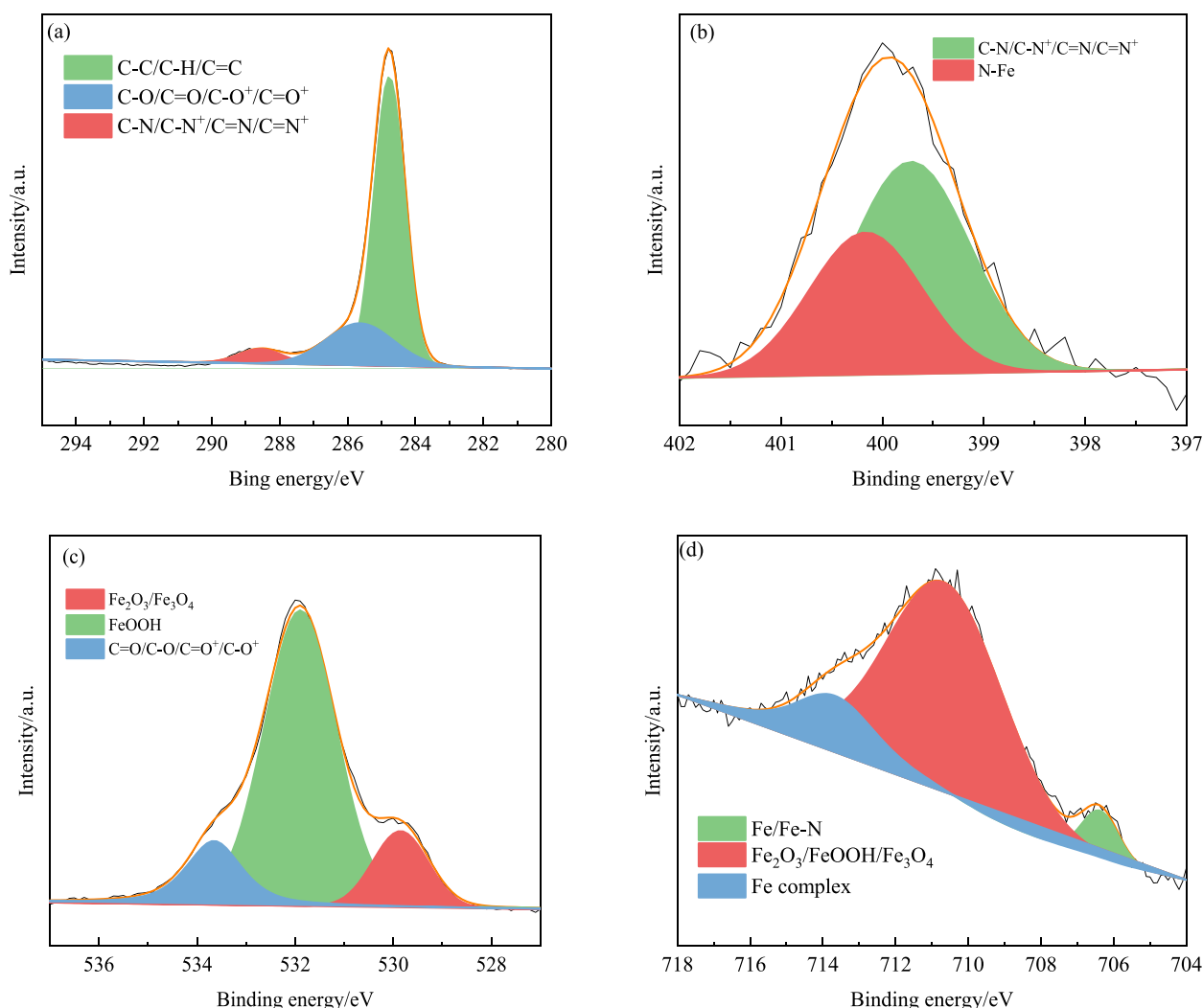


Fig. 5. High-resolution XPS spectra of elements in the IBLE adsorption film. (a) C 1s, (b) N 1s, (c) O 1s, and (d) Fe 2p_{3/2}.

C-O⁺ (Attou et al., 2020), consistent with the C 1s results. It further implies that the active components in IBLE are adsorbed on the MS surface.

As shown in Fig. 5d, the Fe 2p_{3/2} spectrum consists of three types of distinct compounds. The minor peak at 706.4 eV may correspond to Fe 2p_{3/2} in the Fe-N bond (Chrysochoou et al., 2018) or simple Fe (i.e. Fe⁰) (Ahmed and Zhang, 2020). The presence of matrix iron implies an imperfect adsorption film of IBLE, whereas the existence of Fe-N bonds indicates the adsorption of active components. The second strong peak at 710.6 eV can be attributed to Fe 2p_{3/2} in Fe₂O₃, Fe₃O₄, and FeOOH (Berrissoul et al., 2022; Hashim et al., 2019). The presence of FeOOH and Fe₂O₃ indicates that the IBLE components are advantageous for forming stable Fe³⁺ oxides to enhance corrosion resistance (Zarrok et al., 2012). The third satellite peak at 713.9 eV may be related to iron complexes (Alreth et al., 2021). The organic matter in IBLE may act as electron donors and/or electron acceptors, sharing electrons with iron atoms/ions and generating iron complexes. Moreover, the protonated molecules shown in Fig. 2 can be adsorbed onto the MS surface via electrostatic attraction. Therefore, the formation of iron compounds and the adsorption of active components improve the corrosion resistance of steel in a 1 M HCl solution.

4.2. Surface morphology of the corroded steel

The surface morphology of MS immersed in 1 M HCl solutions with different concentrations of IBLE was shown in Fig. 6. The MS sample is seriously corroded in the absence of IBLE, and many interpenetrating and deep pits are distributed on the surface. The corrosion pits are noticeably reduced in the presence of 1.0 g/L IBLE, but some are still deep. When the IBLE concentration increased to 5.0 g/L, MS corrosion was significantly inhibited, and the pits almost vanished. Careful observation demonstrates a fuzzy film on the MS surface in the presence of IBLE, and the clarity becomes more apparent at 5.0 g/L IBLE. The SEM observations reveal that an appropriate concentration of IBLE can effectively slow down the corrosion of MS in a 1 M HCl medium.

4.3. Electrochemical corrosion behaviours

4.3.1. Open circuit potential (OCP) curves

The dynamic equilibrium tendency of the electrode reactions in a corrosion system can be detected by the OCP test (Pal and Das, 2022). The effect of IBLE concentrations on the OCP-time curves of the MS samples in 1 M HCl solutions at 298, 308, and 318 K was shown in Fig. 7.

As depicted in Fig. 7a, in the blank solution at 298 K, at the beginning stage, the OCP of MS fluctuates significantly. It firstly increases and at 300 s turns to decrease continuously. It becomes nearly stable for immersion time longer than 2400 s, indicating that the electrode system at this time has almost reached the dynamic equilibrium. In the presence of IBLE at 298 K, the electrode system also achieves dynamic equilibrium after almost 2400 s. The IBLE inhibitor leads to a positive shift in the near-stable OCP compared to the blank solution. However, the difference is less than 30 mV. A change amplitude in electrode potential above

85 mV would indicate that it is either the anodic or cathodic corrosion inhibitor (Liao et al., 2023; Satapathy et al., 2009). Therefore, at 298 K, IBLE acts as a mixed corrosion inhibitor for MS with a little greater influence on the anodic process.

As illustrated in Fig. 7b and 7c, the change laws of the OCP with immersion times at 308 and 318 K are similar to those at 298 K. However, OCP tends to stabilize faster at 308 and 318 K. In other words, the electrode system achieves the dynamic equilibrium more rapidly. Compared to the blank solution at 308 K, the near-stable OCP fluctuates in both the positive and negative directions, which is related to the IBLE concentrations. However, at 318 K, OCP shifts in a more negative direction with increased IBLE concentrations. Similar to 298 K, the OCP difference in the absence and presence of IBLE at 308 and 318 K is also less than 30 mV. IBLE remains a mixed corrosion inhibitor for MS at 308 and 318 K. However, the cathode control in the mixed inhibition is slightly superior at 318 K. The slight difference between the anode and cathode controls in mixed inhibition may be related to the change in adsorption types, such as physical, chemical, and mixed adsorption, with temperature (Lin et al., 2023).

4.3.2. Potentiodynamic polarization (PDP) curves

The PDP curves for MS in 1 M HCl solutions with various concentrations of IBLE at 298, 308, and 318 K are illustrated in Fig. 8. The corresponding polarization parameters are shown in Table 1.

As depicted in Fig. 8a, in the blank solution without IBLE at 298 K, both the anode and cathode polarization curves of MS display the characteristics of activated polarization, in which the anode reaction is the dissolution of steel and the cathode reaction is the hydrogen evolution process. With the addition of IBLE, both the anode and cathode polarization current densities of MS decrease dramatically, and the polarization branches shift to the left. IBLE significantly inhibits both the oxidation dissolution of iron and the reduction of hydrogen ions. This can be attributed to the adsorption of organic components on the MS surface, as confirmed by the results of chemical compositions and surface morphology in Figs. 3–5. When the IBLE concentration was increased to 0.1 g/L, the cathode branch migrates to the left by almost an order of magnitude. With 3.0 g/L IBLE, the cathode branch continuously moves slightly to the left. However, it remains unchanged when the IBLE concentration was increased to 5.0 g/L. The anode polarization curve shifts noticeably to the left with 0.1 g/L IBLE, but it essentially remains unchanged with IBLE content in the range from 0.1 to 1.0 g/L. With higher IBLE content, the anode curve moves to the left. Similarly, this might be related to the proportional change in the adsorption types, such as physical, chemical, and mixed adsorption (Pereira et al., 2012). In addition, after adding IBLE to a 1 M HCl solution at 298 K, the shape of the anode and cathode polarization curves remains almost invariant, and the activation polarization still controls the corrosion processes. The corrosion mechanism of MS in a 1 M HCl solution is not altered, and IBLE exhibits the inhibition effect of geometric coverage.

As illustrated in Fig. 8a, a minimal addition of IBLE (i.e., 0.1 g/L) to a 1 M HCl solution causes a significant left-shift of the cathode and anode polarization branches. The protonated onium ions of the organic

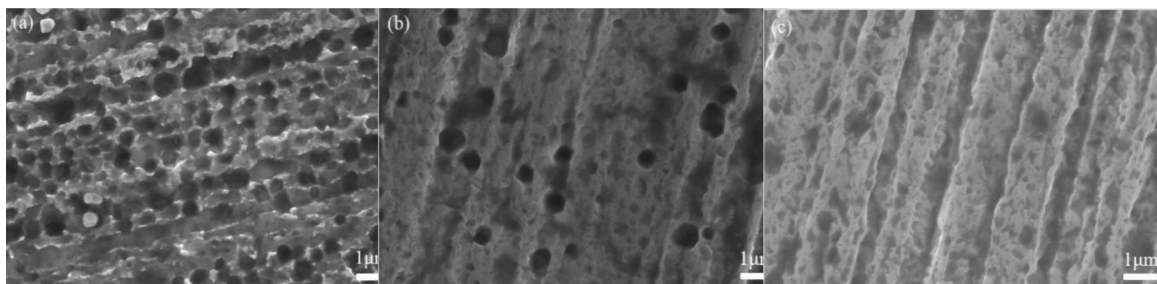


Fig. 6. Surface morphology of MS in 1 M HCl solutions with various concentrations of IBLE: (a) without, (b) with 1.0 g/L, and (c) with 5.0 g/L.

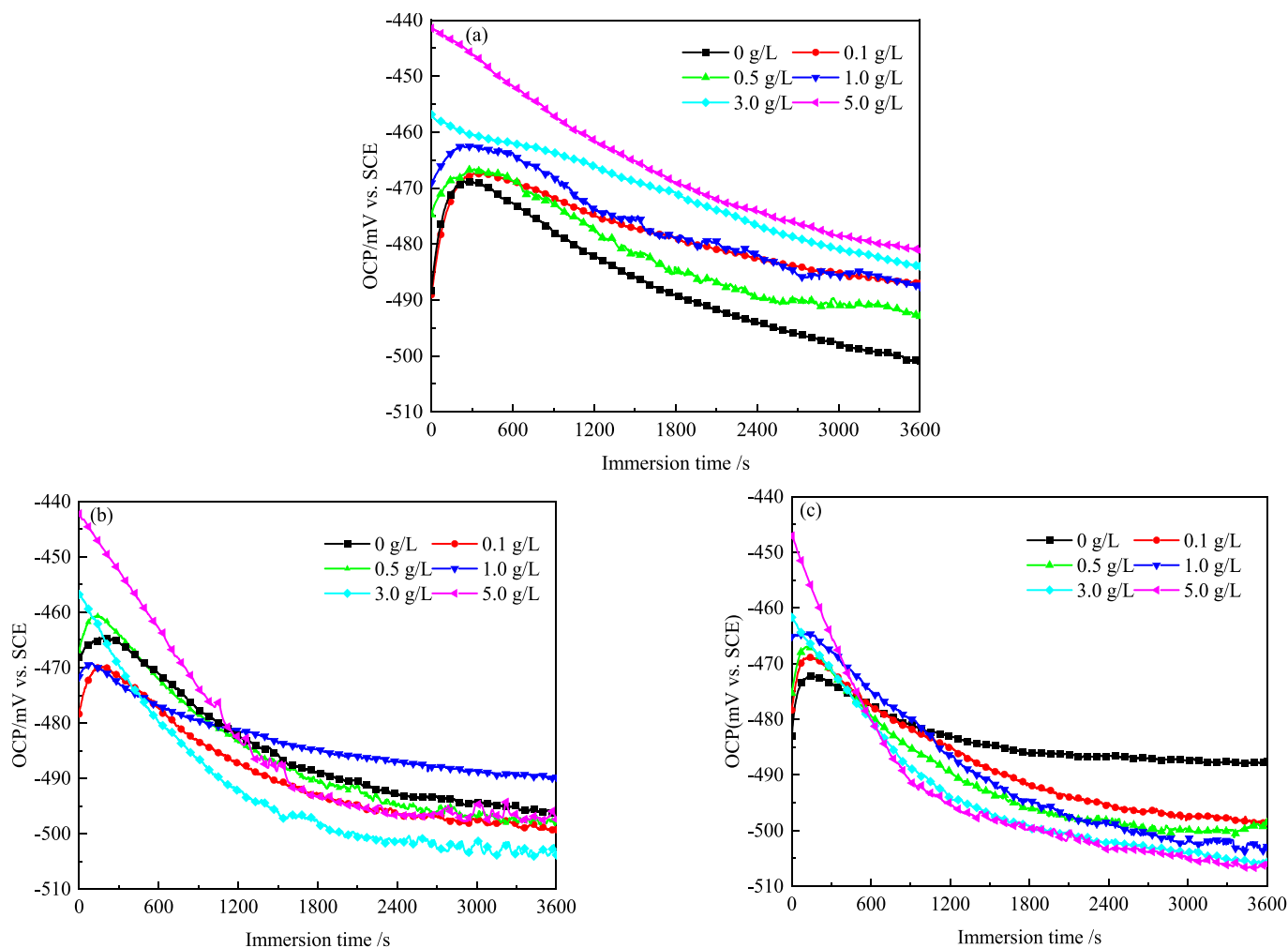


Fig. 7. OCP–time curves of MS in 1 M HCl solutions with different concentrations of IBLE at (a) 298, (b) 308, and (c) 318 K.

compounds in IBLE, which are positively charged (Fig. 2), can preferentially adsorb on the cathodic active sites of MS through electrostatic attraction, forming an adsorption film to mechanically isolate the contact between steel and solution. The corrosion reaction is inhibited. Meanwhile, the neutral and protonated active ingredients in IBLE may also be adsorbed onto the surface of MS via van der Waals forces and/or electron sharing. The plant components such as vitamin B2, quercetin, and protocatechualdehyde possess many π electrons and lone pair electrons, while iron has unfilled and filled $3d$ orbitals. During the coordination sharing of electron donation and reception, the active components invariably adsorb onto the steel surface, forming iron complexes and an adsorption film. The steel and the solution are also isolated automatically. With increasing the IBLE concentration, the electrostatic attraction adsorption of protonated compounds on the cathodic active sites gradually becomes saturated. Therefore, the left shift amplitude of the cathodic polarization branch gradually weakens. However, the anodic branch left-shifts continuously. This may be due to the oxidation reaction of Fe^{2+} near the anode into Fe^{3+} and the formation of dense trivalent iron oxides and hydroxides.

As illustrated in Fig. 8, the influence of the IBLE concentration on the PDP curves at 298, 308, and 318 K is similar, and the corrosion inhibition at 308 and 318 K is also a geometric coverage effect. However, as the solution temperature increases, the corrosion inhibition of IBLE on the cathode reaction of MS is greater than that on the anode process, leading to a negative shift in E_{cor} . The adsorption by electrostatic attraction between the protonated molecules and cathode active points may be somewhat enhanced.

Based on the geometric coverage effect of IBLE for MS in a 1 M HCl solution, the coverage based on the PDP test (θ_{PDP}) can be calculated by the following expression (Silva et al., 2021; Umoren et al., 2014):

$$\theta = \frac{\eta_{\text{PDP}}}{100} \quad (2)$$

As shown in Table 1, with an increase in the IBLE concentration, the variation rules of the polarization parameters of MS at 308 and 318 K are nearly identical to those at 298 K. However, the degree of decline in i_{cor} increases with the solution temperature and the IBLE concentration (higher than 0.5 g/L). Therefore, η_{PDP} and θ_{PDP} boost with the solution temperature and the IBLE content. It suggests that the enhancement in η_{PDP} of IBLE for MS is higher than the acceleration corrosion rate of MS. At 298, 308, and 318 K, η_{PDP} is up to 94.9 %, 95.6 %, and 96.4 % with 5.0 g/L IBLE. It suggests that IBLE is an excellent corrosion inhibitor for MS in a 1 M HCl solution. Notably, η_{PDP} is enhanced with increasing the solution temperature, but the corrosion rate of MS is still much higher than that at 298 K. Reducing the medium temperature plays a vital role in decreasing the corrosion rate of steel. Therefore, the relevant experiments were not performed at higher temperatures in this study.

4.3.3. Electrochemical impedance spectroscopy (EIS) diagrams

The EIS diagrams of MS in 1 M HCl solutions with different concentrations of IBLE at 298, 308, and 318 K are shown in Figs. 9–11, respectively. As illustrated in Fig. 9, regardless of whether IBLE was added to a 1 M HCl solution at 298 K, the Nyquist diagram contains only one deformed capacitance arc. The negative phase angle-logf curve in

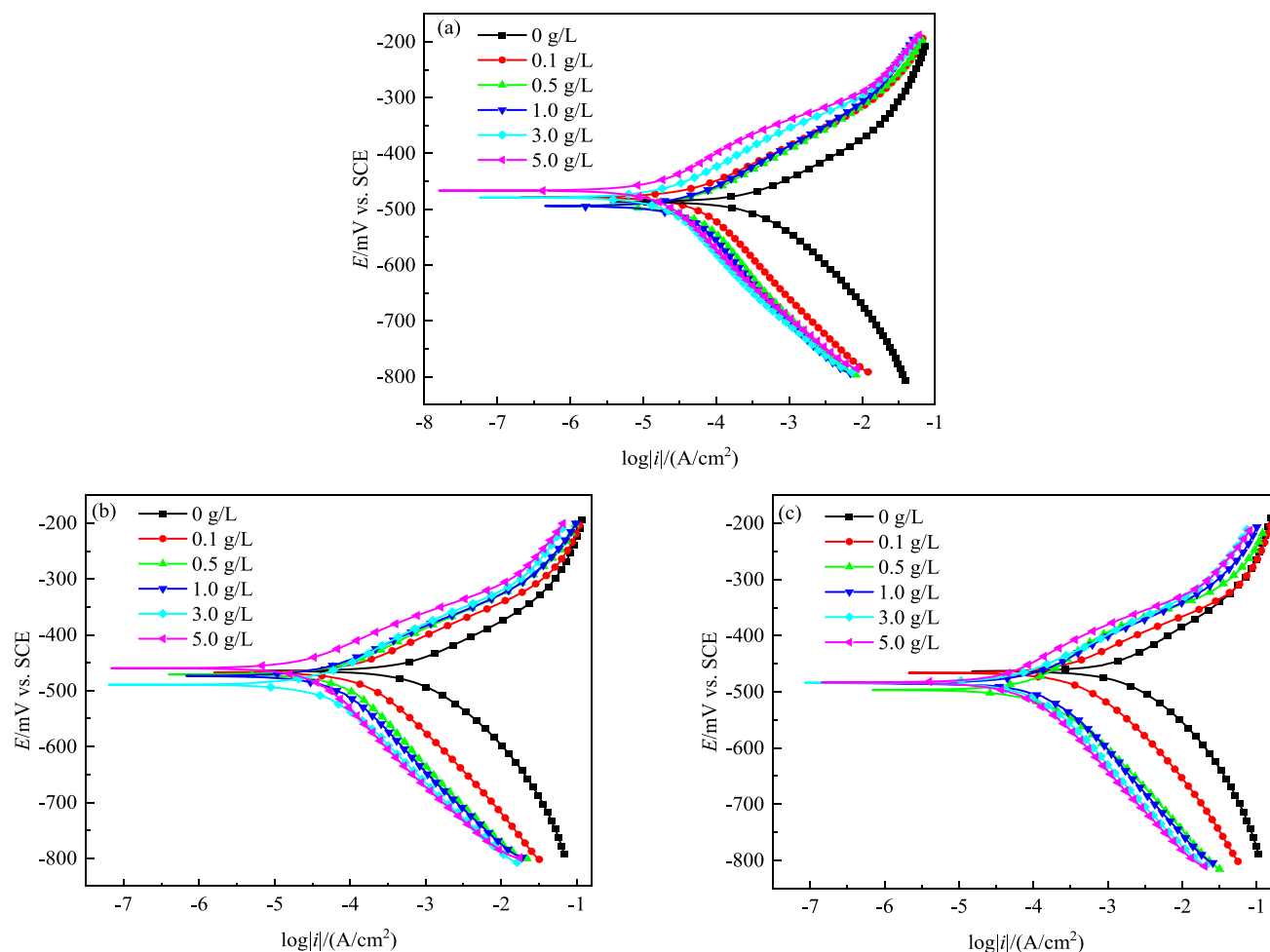


Fig. 8. PDP curves of MS in 1 M HCl solutions with different IBLE contents at (a) 298, (b) 308, and (c) 318 K.

Table 1

Effect of IBLE concentration on polarization parameters of MS in 1 M HCl solutions at different temperatures.

T/ K	C_{inh} / (g/L)	E_{cor} /mV vs. SCE	b_c /(mV/ dec)	b_a / (mV/ dec)	i_{cor} ($\times 10^{-5}$)/ (A/ cm^2)	η_{PDP} / %	θ_{PDP}
298	0	-487	-117	49	30.0	-	-
	0.1	-479	-144	65	4.73	84.3	0.843
	0.5	-488	-161	72	4.40	85.4	0.854
	1.0	-495	-158	74	3.69	87.7	0.877
	3.0	-480	-146	72	1.88	93.7	0.937
	5.0	-467	-137	68	1.54	94.9	0.949
308	0	-465	-119	76	63.6	-	-
	0.1	-468	-126	59	12.7	80.1	0.801
	0.5	-472	-146	61	7.14	88.8	0.888
	1.0	-474	-138	57	5.12	92.0	0.920
	3.0	-489	-131	63	3.63	94.3	0.943
	5.0	-460	-147	51	2.80	95.6	0.956
318	0	-463	-126	84	135.9	-	-
	0.1	-467	-122	55	31.1	77.1	0.771
	0.5	-497	-120	78	9.24	93.2	0.932
	1.0	-485	-131	64	9.50	93.0	0.930
	3.0	-484	-134	70	6.78	95.0	0.950
	5.0	-483	-1328	60	4.93	96.4	0.964

the Bode diagram merely has one narrow peak. It demonstrates that the entire electrode system has one-time constant (Rathod et al., 2022). The single capacitance arc and the single time constant can be attributed to the electric double-layer capacitance of the interface between MS and solution, while the deformed capacitance arc and the negative phase

angle peak of less than 90° can be attributed to the dispersion effect due to the heterogeneity of the electrode surface (Li et al., 2021; Mourya et al., 2014). With increasing IBLE concentration in a 1 M HCl solution at 298 K, the radius of the capacitance arc and the impedance modulus at low frequency improve dramatically, as do the height and half-height width of the peak of the negative phase angle. These phenomena suggest that adsorption and coverage of active components on the MS surface are improved, enhancing charge-transfer resistance of corrosion reaction and reducing electric double-layer capacitance. Thus, the protection efficiency of adsorption film for steel is heightened. Moreover, adding IBLE does not change the shapes of EIS diagrams. It again implies that the corrosion mechanism of MS is not altered, and IBLE manifests an inhibition mechanism of geometric coverage effect (Asadi et al., 2019; Li et al., 2019; Mourya et al., 2014).

As shown in Figs. 9–11, the influence of the IBLE concentrations on the EIS diagrams at 308 and 318 K is almost the same as that at 298 K. The corrosion mechanism of MS at 308 and 318 K is also unaffected by IBLE. However, with an increase in the medium temperature, the radius of the capacitance arc in the Nyquist diagrams and the impedance modulus at low frequencies in the Bode diagrams decrease significantly. The charge-transfer resistance of MS decreases, and the corrosion rate increases with medium temperature. Additionally, the peak height of the negative phase angle decreases, and the corresponding characteristic frequency increases, leading to an increase in the electric double-layer capacitance.

Fig. 12 shows a typical equivalent circuit for analysing the EIS diagrams in Figs. 9–11 (Bidi et al., 2021; Salmasifar et al., 2021). R_s is the solution resistance, R_{ct} is the charge-transfer resistance of MS, and CPE-

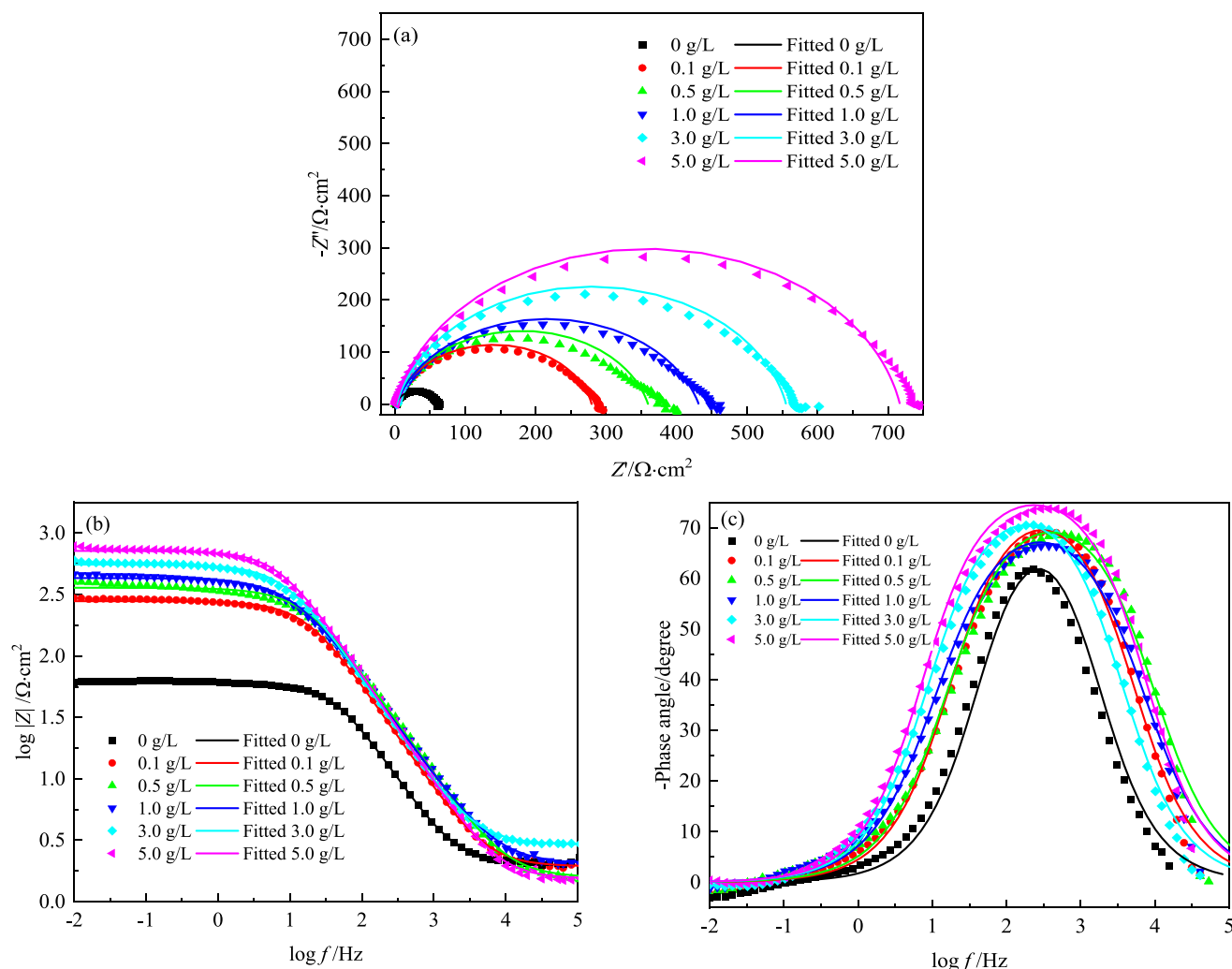


Fig. 9. EIS of MS in 1 M HCl solutions containing different concentrations of IBLE at 298 K: (a) Nyquist diagrams, (b)(c) Bode diagrams.

d_l is the electric double-layer capacitance of the MS/solution interface, which was expressed as (Eid et al., 2020; Fernandes et al., 2019):

$$Z_{CPE-dl} = \frac{1}{Y_{0-dl}(j\omega)^{n_{dl}}} \quad (3)$$

where Y_{0-dl} is the auxiliary parameter related to the capacitance value, ω is the angular frequency, and j is the imaginary component. n_{dl} illustrates the distortion degree of the electric double-layer capacitance, which ranges from 0 to 1. When n_{dl} was 1, CPE-dl behaved as the ideal plate capacitance. The electric double-layer capacitance, denoted as C_{dl} , was calculated as the following expression suggested by Hsu and Mansfeld (Hsu and Mansfeld, 2001):

$$C_{dl} = Y_{0-dl} \cdot (\omega_{max})^{n_{dl}-1} = Y_{0-dl} \cdot (2\pi f_{max})^{n_{dl}-1} \quad (4)$$

where ω_{max} is the characteristic angular frequency, and f_{max} is the characteristic frequency corresponding to the maximal imaginary part in the Nyquist diagram.

Table 2 lists the EIS fitting parameters for MS at 298, 308, and 318 K. The corrosion protection efficiency based on the EIS tests, denoted as η_{EIS} , was determined by (Chen et al., 2020; Zakaria et al., 2022)

$$\eta_{EIS} = \frac{R_{ct} - R_{ct,0}}{R_{ct}} \times 100\% \quad (5)$$

where $R_{ct,0}$ and R_{ct} are the charge-transfer resistances of MS in 1 M HCl

solutions with and without IBLE, respectively. Similarly, the coverage based on the EIS test, denoted as θ_{EIS} , was calculated according to formula (2).

As shown in Table 2, with increasing IBLE concentration in a 1 M HCl solution at 298 K, R_{ct} is obviously improved, and so are η_{EIS} and θ_{EIS} . This can be attributed to the adsorption of the active components such as D-mannose, vitamin B2, quercetin, and protocatechualdehyde on the MS surface, effectively blocking the corrosion attack of HCl for MS. n_{dl} is roughly 0.83 ~ 0.90, close to 1. It indicates that the electric double-layer capacitance of the interface between MS and solution is close to the ideal flat capacitor. n_{dl} is marginally dropped after IBLE was added. When the hydrophilic groups in IBLE were adsorbed on the MS surface, the hydrophobic groups in IBLE deviated from the steel surface, increasing the roughness and uniformity. Additionally, Y_{0-dl} fell as IBLE concentration increased. Compared with the blank solution without IBLE, C_{dl} decreases, but the overall decrease degree does not increase significantly with extract concentration. Once again, it demonstrates the corrosion inhibition mechanism of the geometric coverage effect of IBLE. According to the Helmholtz model $C = \epsilon^0 \epsilon S/d$ (El-Hashemy and Sallam, 2020; Li et al., 2021), the reasons for the adsorption of IBLE active molecules on the MS surface make the decrease in C_{dl} can be clarified as follows: 1) The original water molecules with higher dielectric constant were replaced, leading to the decreases in ϵ ; 2) The flat plate space d of the electric double-layer capacitance was increased due to the larger size of the organic molecules; and 3) The real surface area S of the capacitor was reduced because of the enhancement of the

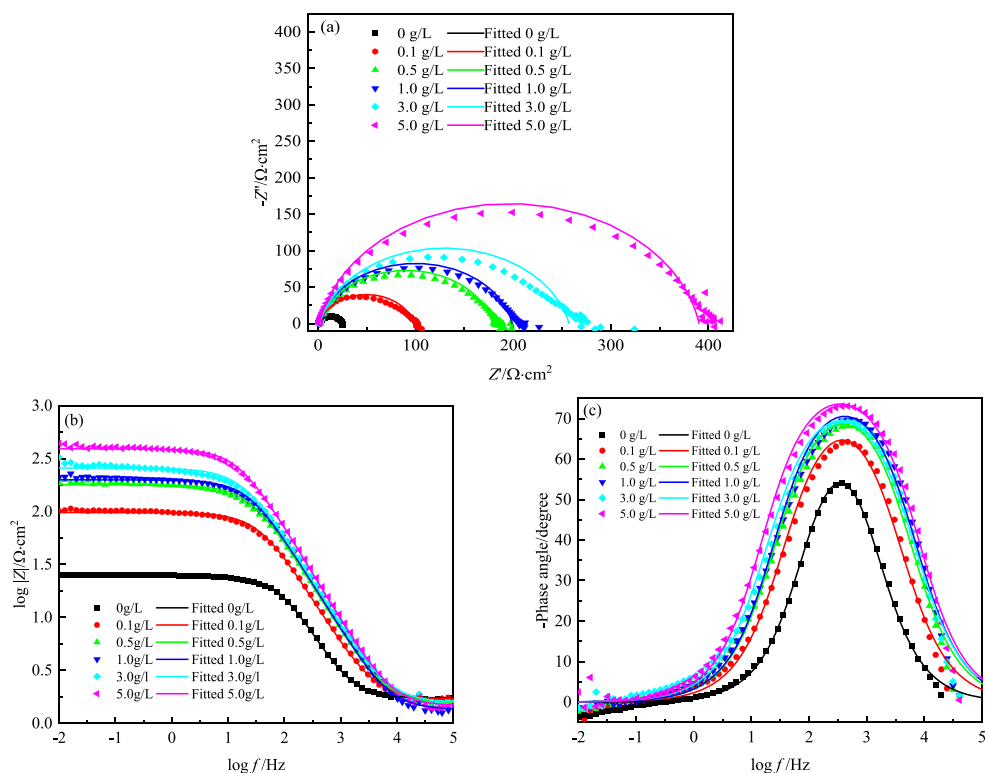


Fig. 10. EIS of MS in 1 M HCl solutions containing different concentrations of IBLE at 308 K: (a) Nyquist diagrams, (b)(c) Bode diagrams.

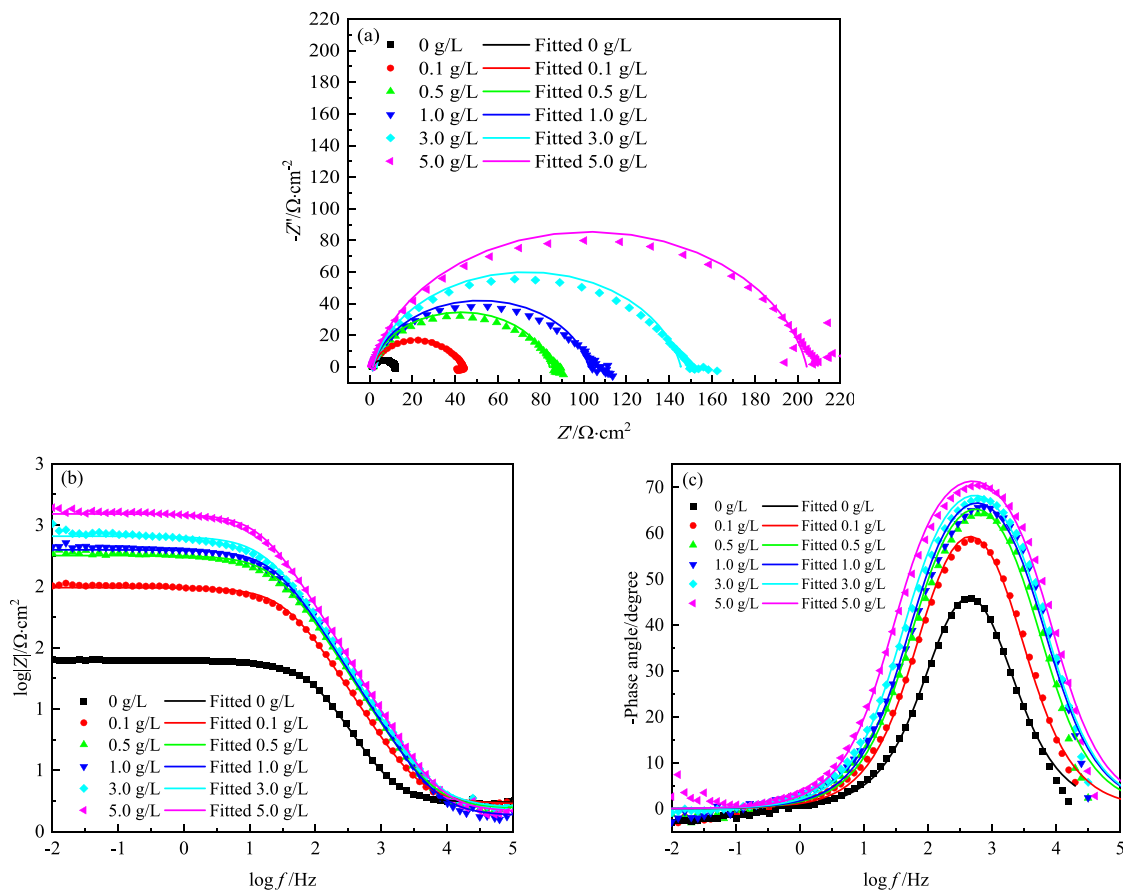


Fig. 11. EIS of MS in 1 M HCl solutions containing different concentrations of IBLE at 318 K: (a) Nyquist diagrams, (b)(c) Bode diagrams.

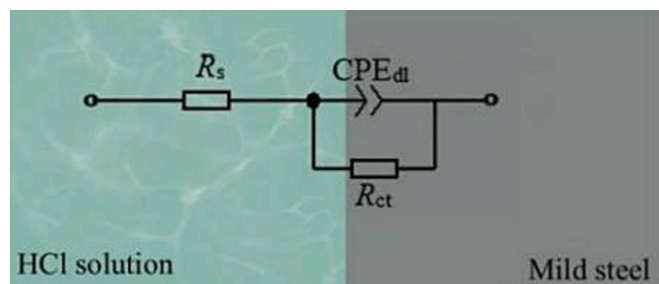


Fig. 12. Equivalent circuit for analysing EIS diagrams.

compactness of the adsorption film.

As shown in Table 2, the variation rules of the impedance parameters with the IBLE concentration at 308 and 318 K are nearly the same as those at 298 K. The maximal test concentration of IBLE in this study was 5.0 g/L. The corresponding η_{EIS} at 298, 308, and 318 K is 91.7 %, 94.1 %, and 94.8 %, respectively. η_{EIS} increases with the solution temperature. However, R_{ct} of MS decreases noticeably with an increase in solution temperature. This is in good agreement with the PDP results.

4.4. Adsorption behaviours

4.4.1. Adsorption isotherms

The adsorption capacity of organic molecules on metal surfaces is an essential standard for measuring corrosion inhibition effectiveness (Ituen et al., 2017). The interaction between the inhibitor molecules and the metal surface can be inferred from the adsorption isotherms (Fernandes et al., 2019). Three adsorption isotherm equations were tried according to θ_{PDP} and θ_{EIS} in Tables 1 and 2.

Langmuir isotherm (Bhardwaj et al., 2021; Chen et al., 2020; Dehghani et al., 2019b):

$$\frac{C_{\text{inh}}}{\theta} = \frac{1}{K_{\text{ads}}} + C_{\text{inh}} \quad (6)$$

El-Awady isotherm (Bhardwaj et al., 2022):

$$\ln \frac{\theta}{1-\theta} = \ln K_{\text{ads}} + y \ln C_{\text{inh}} \quad (7)$$

Temkin isotherm (Pal and Das, 2022; Saini et al., 2018):

$$\theta = -\frac{1}{2\alpha} \ln C_{\text{inh}} - \frac{1}{2\alpha} \ln b \quad (8)$$

where θ is the coverage of IBLE on the MS surface, i.e. θ_{PDP} and θ_{EIS} in Tables 1 and 2, respectively. C_{inh} is the mass concentration of IBLE in 1

M HCl solution (g/L). K_{ads} is the adsorption equilibrium constant (L/g), which can be calculated from the intercepts of the Langmuir and El-Awady isotherms. y indicates the number of water molecules replaced by one inhibitor molecule. b is the Temkin isotherm constant. α indicates the interaction force between inhibitor molecules in the adsorption film. A negative value of α indicates a repulsive force, while a positive value indicates mutual attraction (Liu et al., 2023).

The fitting results for three adsorption isotherms are shown in Figs. 13–15 and Table 3. The adsorption of the IBLE molecules on the MS surface in a 1 M HCl solution at 298, 308, and 318 K strictly follows the Langmuir isotherm, but it does not satisfy the El-Awady and Temkin isotherms. The adsorption film on the MS surface is a mono-molecular layer with no interaction force between molecules (Lin et al., 2023; Silva et al., 2021). This coincides with the EIS diagram, which has only one capacitance arc and one time constant, confirming the above results of the chemical compositions and surface morphology.

K_{ads} represents the ability of organic molecules to adsorb onto a metal surface (Berrissoul et al., 2022; Younes et al., 2017; Zuo et al., 2021). When K_{ads} is higher, the adsorption capacity of the inhibitor molecules is stronger, resulting in better corrosion inhibition efficiency. As shown in Table 3, K_{ads} based on the PDP test increases significantly with the solution temperature, whereas that based on the EIS test shows little change. This difference is related to the distinct electrochemical testing principles and the different calculation methods of η (as shown in Tables 1 and 2). The corrosion rate of MS increases at higher temperatures; however, the adsorption ability of the active molecules on the MS surface, i.e., θ , is enhanced. This confirms the enhancement in η of IBLE for MS with increasing solution temperature (as shown in Tables 1 and 2). Moreover, the Langmuir isotherms based on PDP and EIS results were very similar. The two electrochemical tests did not affect the evaluation of the adsorption performance and parameters of IBLE on the MS surface.

4.4.2. Adsorption parameters

To further explore the adsorption behaviours of IBLE on the MS surface, the Gibbs free energy of adsorption, denoted as ΔG_{ads} was calculated as (Chen et al., 2020; Li et al., 2021; Younes et al., 2017):

$$K_{\text{ads}} = \frac{1}{\rho_{\text{solvent}}} \exp\left(-\frac{\Delta G_{\text{ads}}}{RT}\right) \quad (9)$$

where K_{ads} is the equilibrium adsorption constant (L/g), as listed in Table 3. R is the gas constant (8.314 J/K), T is the Kelvin temperature (K), ρ_{solvent} is the mass concentration of water solvent in the corrosion system (g/L). IBLE concentration was relatively low, ρ_{solvent} of 1 M HCl solution was approximately 962 g/L.

Table 2

EIS fitted parameters of MS in 1 M HCl solutions with different concentrations of IBLE.

T/K	$C_{\text{inh}}/(\text{g/L})$	$R_s/(\Omega \cdot \text{cm}^2)$	$Y_{0\text{-dl}}(\times 10^{-5})/(\Omega^{-1} \cdot \text{cm}^{-2} \cdot \text{s}^{-n})$	n_{dl}	$R_{\text{ct}}/(\Omega \cdot \text{cm}^2)$	$f_{\text{max}}/(\text{Hz})$	$C_{\text{dl}}(\times 10^{-5})/(\text{F}/\text{cm}^2)$	$\eta_{\text{EIS}}/(\%)$	θ_{EIS}
298	0	2	11.2	0.899	59.5	28.27	6.6	–	–
	0.1	2	5.9	0.875	277.6	18.00	3.3	78.6	0.786
	0.5	2	5.6	0.848	357.9	18.00	2.7	83.4	0.834
	1.0	2	6.9	0.829	429.3	11.25	3.3	86.1	0.861
	3.0	3	5.5	0.872	552.4	8.82	3.3	89.2	0.892
	5.0	2	4.7	0.885	715.1	7.03	3.0	91.7	0.917
308	0	2	13.9	0.920	22.9	91.53	8.4	–	–
	0.1	2	8.7	0.878	96.1	45.00	4.4	76.2	0.762
	0.5	2	6.5	0.887	177.3	28.27	3.6	87.1	0.871
	1.0	1	5.8	0.885	197.5	22.31	3.3	88.4	0.884
	3.0	2	6.3	0.867	255.6	22.31	3.3	91.1	0.911
	5.0	2	4.4	0.894	389.0	14.06	2.7	94.1	0.941
318	0	1	24.4	0.892	10.6	144.97	11.7	–	–
	0.1	2	9.7	0.899	40.7	72.00	5.2	73.9	0.739
	0.5	2	6.5	0.872	82.6	56.84	3.1	87.2	0.872
	1.0	1	6.0	0.884	101.0	45.00	3.1	89.5	0.895
	3.0	2	5.1	0.885	143.8	45.00	2.7	92.6	0.926
	5.0	1	4.8	0.891	203.0	28.27	2.7	94.8	0.948

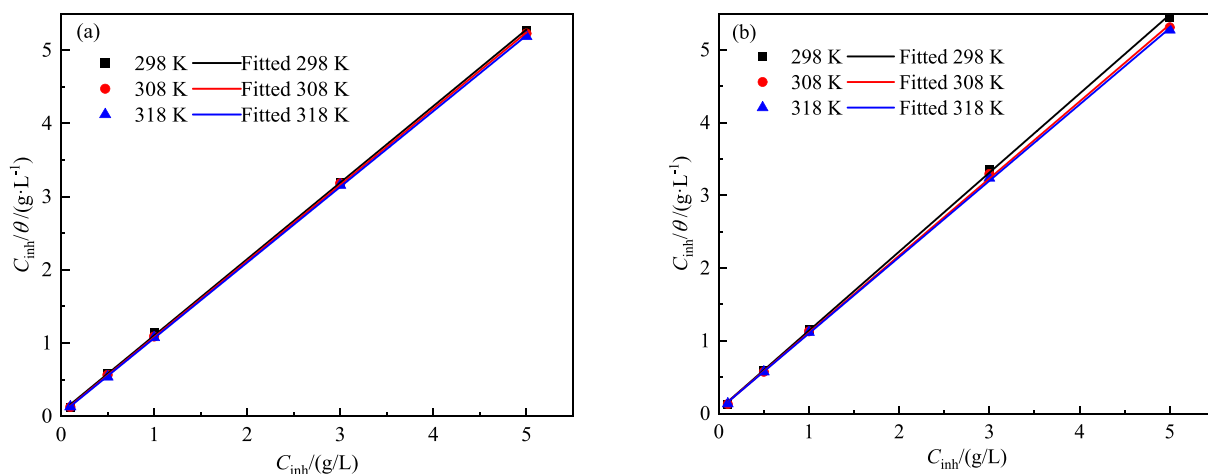


Fig. 13. Langmuir adsorption isotherms of IBLE on the MS surface based on (a) PDP and (b) EIS tests.

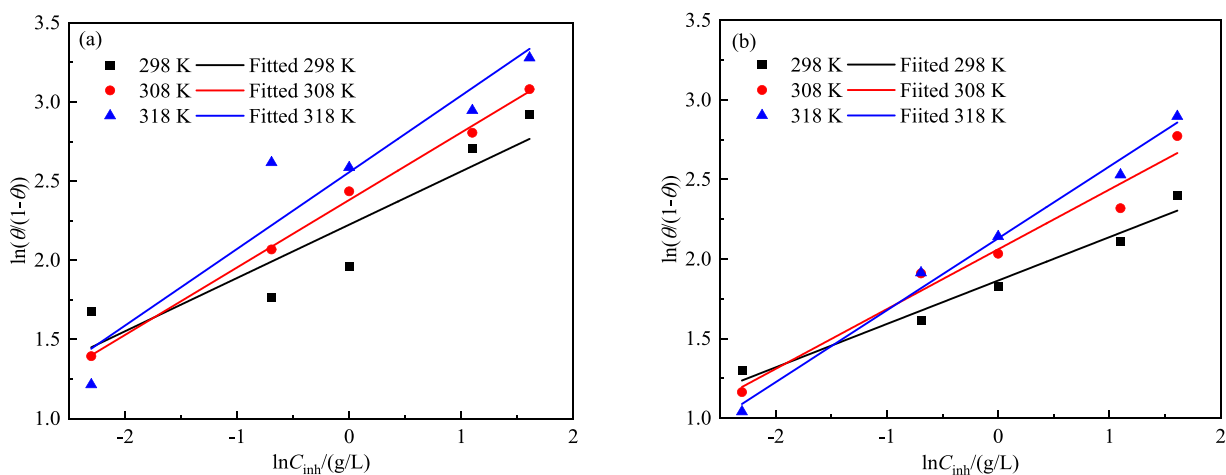


Fig. 14. El-Awady adsorption isotherms of IBLE on the MS surface based on (a) PDP and (b) EIS tests.

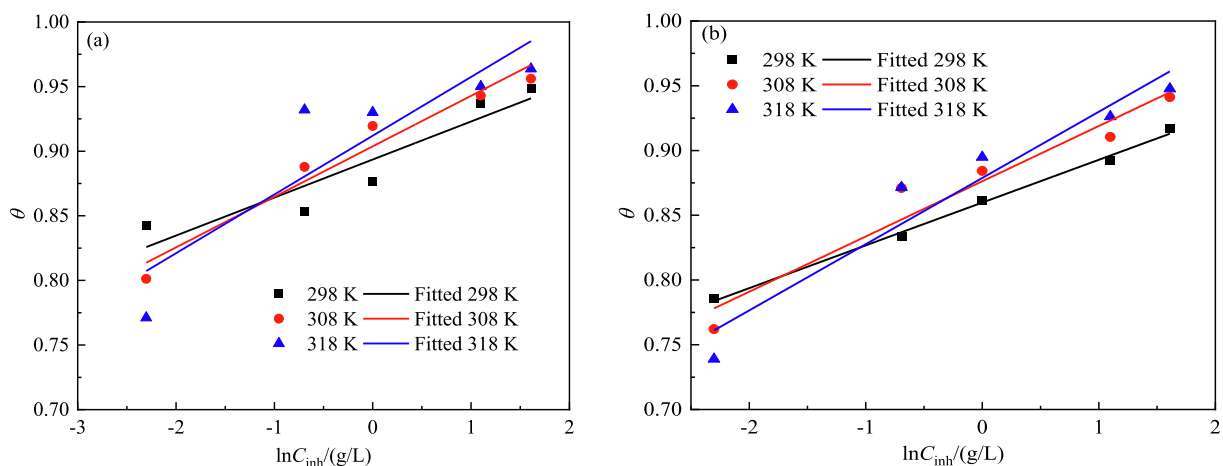


Fig. 15. Temkin adsorption isotherms of IBLE on the MS surface based on (a) PDP and (b) EIS tests.

Generally, when ΔG_{ads} was negative and higher than -20 kJ/mol, it is physically adsorbed; when ΔG_{ads} was smaller than -40 kJ/mol, it is chemisorbed (Tan et al., 2019; Wang et al., 2022). When ΔG_{ads} was in the range of $-40 \sim -20$ kJ/mol, it is mixed adsorption of physical adsorption and chemisorption. As shown in Table 3, all ΔG_{ads} at 298, 308, and 318 K are negative and range from -27.4 to -24.3 kJ/mol. The

adsorption of active molecules in IBLE on the MS surface is spontaneous, and the mixed adsorption is dominated by physical adsorption. Moreover, as the temperature of the solution increases, ΔG_{ads} is enhanced. This further supports an increase in the adsorption capacity of the active molecules in IBLE. ΔG_{ads} based on the PDP test are slightly higher than that obtained from the EIS test at a fixed temperature.

Table 3
Fitting results of Langmuir adsorption isotherm of IBLE on the MS surface.

Test method	T/K	R ²	Intercept	Slope	K _{ads} /(L/g)	ΔG _{ads} /(kJ/mol)
PDP	298	0.9998	0.056	1.045	17.9	-24.3
	308	1.0000	0.039	1.041	25.7	-26.0
	318	0.9999	0.032	1.034	31.4	-27.4
EIS	298	0.9997	0.055	1.086	18.0	-24.3
	308	0.9997	0.055	1.059	18.3	-25.1
	318	0.9999	0.053	1.049	18.7	-26.0

According to Faraday's law and i_{cor} in Table 1, the corrosion rate of MS (v) was calculated by the following expression (Mansfeld, 2005):

$$v = \frac{Mi_{\text{cor}}}{nF} \quad (10)$$

where M is the relative atomic weight of MS, i.e. 56 g/mol. n is the number of exchanged charges for the oxidation reaction of Fe, i.e. 2. F is the Faraday constant, i.e. 26.8 A·h.

According to the Arrhenius and Transition-state theory, the influence of IBLE on the kinetic parameters of corrosion processes of MS in 1 M HCl solution was analysed (Benghalia et al., 2018; Tang et al., 2021).

Arrhenius equation:

$$\ln v = \ln A - \frac{E_a}{RT} \quad (11)$$

Transition-state equation:

$$\ln\left(\frac{v}{T}\right) = -\frac{\Delta H_a}{RT} + \frac{\Delta S_a}{R} + \ln\left(\frac{R}{Nh}\right) \quad (12)$$

where A is the pre-exponential factor of the Arrhenius equation; E_a is the activation energy of the corrosion reaction of MS; R and T are the same parameters as those in Eq. (9); N is the Avogadro constant, i.e. $6.02 \times 10^{23} \text{ mol}^{-1}$; h is the Plank constant, i.e. $6.626 \times 10^{-34} \text{ J/s}$; ΔH_a and ΔS_a are the activation enthalpy and entropy of the corrosion reaction of MS, respectively.

The fitting results of the Arrhenius and Transition-state equations for the activation reactions of MS in 1 M HCl solutions without and with 5.0 g/L IBLE are illustrated in Fig. 16. The corresponding kinetic parameters are listed in Table 4. The linear fitting results for the two kinetic equations are good. With 5.0 g/L IBLE in 1 M HCl solution, E_a decreases from 59.4 kJ/mol to 45.8 kJ/mol. The slight decrease in E_a can be attributed to the mixed adsorption of D-mannose, vitamin B2, protocatechualdehyde, quercetin, and other active components on the MS surface. A significant decrease in E_a is a characteristic of chemical

Table 4
Kinetic parameters of activation reaction of MS in 1 M HCl solutions without and with 5.0 g/L IBLE.

C _{inh} /(g/L)	A/(g/m ² /h)	E _a /(kJ/mol)	ΔH _a /(kJ/mol)	ΔS _a /(J/mol/K)
0	8.11×10^6	59.4	56.9	-121.2
5.0	1.74×10^3	45.8	43.3	-191.5

adsorption, whereas an increase in E_a is a characteristic of physical adsorption (Rodriguez-Perez et al., 2018). This further confirms that the adsorption of the active components in IBLE on the MS surface follows a combination of physical and chemical adsorption.

The letter A in the Arrhenius equation represents the number of active centres in metal corrosion reactions (Zaher et al., 2022). After adding 5.0 g/L of IBLE into a 1 M HCl solution, A decreases by more than three orders of magnitude. This indicates that the active components in IBLE effectively inhibit the corrosion of MS. Positive values of ΔH_a suggest that the corrosion of MS is an endothermic process (Singh et al., 2011), which verifies the increase in the corrosion rate of MS with the solution temperature. The presence of IBLE leads to a decrease in ΔS_a , indicating a decrease in surface confusion of MS. This can be attributed to the oriented adsorption of active components on the MS surface and the formation of a monolayer adsorption film, in which the interaction force between the molecules is negligible.

4.5. DFT calculation results

To investigate the adsorption behaviour of the active components in IBLE on the surface of MS and to explain the corrosion inhibition mechanism of the geometric coverage effect, the frontier molecular orbital distributions of the active molecules in both neutral and protonated forms were simulated based on the DFT calculations. The relevant energy activity parameters were calculated, including the HOMO energy (E_{HOMO}), the LUMO energy (E_{LUMO}), the energy gap between HOMO and LUMO (ΔE), which reflects the electron stability and molecular reactivity, the ionization potential energy (I), the electron affinity energy (A), the electronegativity (χ), the global hardness (ξ), and ΔN which characterises the electron transfer ability of the organic molecule to metal atoms. The relevant equations are as follows (Bhardwaj et al., 2022; Wang et al., 2022):

$$\Delta E = E_{\text{LUMO}} - E_{\text{HOMO}} \quad (13)$$

$$I = -E_{\text{HOMO}} \quad (14)$$

$$A = -E_{\text{LUMO}} \quad (15)$$

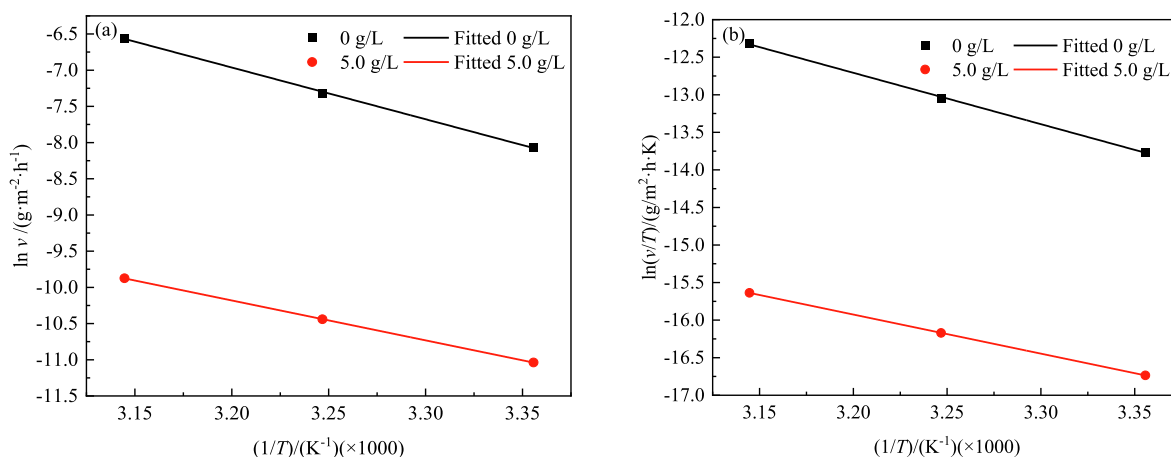


Fig. 16. Fitting lines for the adsorption kinetic equations of MS in 1 M HCl solutions without and with 5.0 g/L IBLE: (a) Arrhenius equation, and (b) Transition-state equation.

$$\chi = \frac{I + A}{2} \quad (16)$$

$$\xi = \frac{I - A}{2} \quad (17)$$

$$\Delta N = \frac{\phi - \chi_{\text{inh}}}{2\xi_{\text{inh}}} \quad (18)$$

where χ_{inh} and ξ_{inh} are the electronegativity and global hardness of the inhibitor molecule, respectively. ϕ is the work function of iron, i.e. 7 eV/mol (Wang et al., 2019).

The HOMO and LUMO distributions of D-mannose, vitamin B2, quercetin, and protocatechualdehyde in neutral and protonated forms are shown in Figs. 17 and 18. The energy activity parameters based on the DFT simulations are listed in Table 5. The differences in the adsorption capacities and corrosion inhibition efficiencies of the four components were quantitatively compared.

As shown in Figs. 17 and 18, HOMO of neutral D-mannose covers almost the entire molecule, exhibiting notable features of electron donors. The lone pair and π electrons tend to donate to the 3d empty orbitals of iron atoms, generating electronic coordination bonds. Neutral D-mannose molecules are thus adsorbed on the MS surface, forming a mechanical barrier film that delays steel corrosion. The LUMO distribution of neutral D-mannose is mainly concentrated at the carbonyl end, where the lone pair electrons can accept the valence electrons from the iron atoms to produce electronic coordination bonds and adsorb on the steel surface. There are filled and unfilled 3d orbitals in the iron atoms.

Neutral D-mannose provides electrons to the 3d unfilled orbitals of iron atoms and receives electrons from the filled 3d orbitals of iron atoms. Therefore, coordination bonds between neutral D-mannose and iron atoms are generated through a synergistic mechanism. The adsorption of neutral D-mannose on the MS surface and the formation of chelates are also realized. After the protonation of D-mannose, LUMO remains unchanged, while HOMO is mainly centred at three hydroxyls far away from carbonyl. The protonation of D-mannose has little effect on its ability to receive electrons but attenuates its electron-donating ability. Although the relative ability of D-mannose to provide and receive electrons in the protonated form is different, the protonated D-mannose molecules still possess synergistic adsorption performance. Moreover, D-mannose has five hydroxyl groups and one carbonyl group with strong polarity. Therefore, electrostatic attraction, directional force, and inductive force are formed between D-mannose and MS surfaces. Physical adsorption occurs. In addition, the protonated D-mannose molecule is positively charged, while the highly active chloride ions can be easily adsorbed on the MS surface, leading to the negative charging of the MS surface. The protonated D-mannose is thus adsorbed, forming an adsorption barrier film. It can be concluded that D-mannose in both neutral and protonated states can be mixed adsorbed on the MS surface by physical and chemical adsorption, confirming the above results of the microscopic and adsorption behaviours.

As shown in Figs. 17 and 18, HOMO and LUMO of neutral vitamin B2 are almost identical and distributed on three aromatic rings and two carbonyls. Protonation has little effect on the HOMO and LUMO distributions of vitamin B2. Many π and lone pair electrons exist in benzene

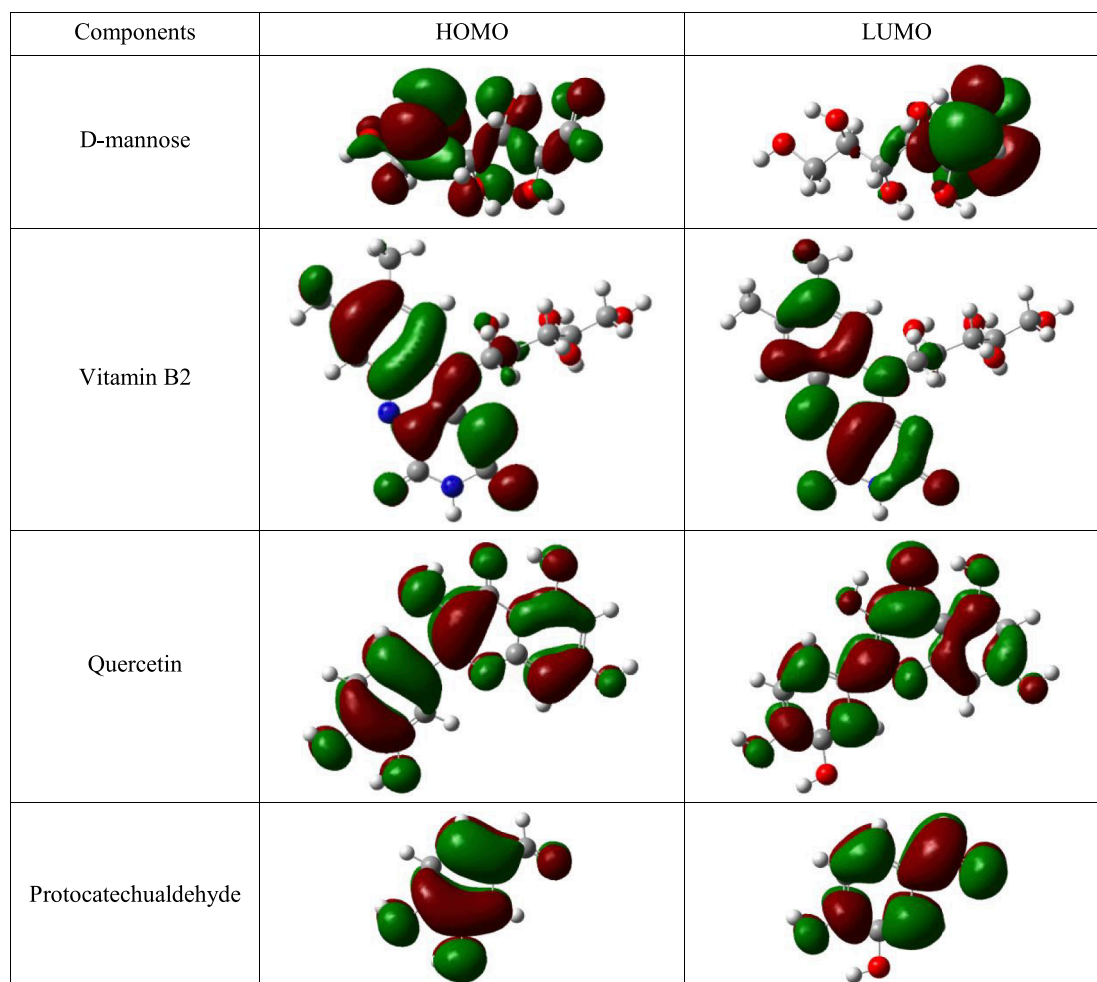


Fig. 17. Frontier molecular orbital distributions of the active components in IBLE in the neutral state.

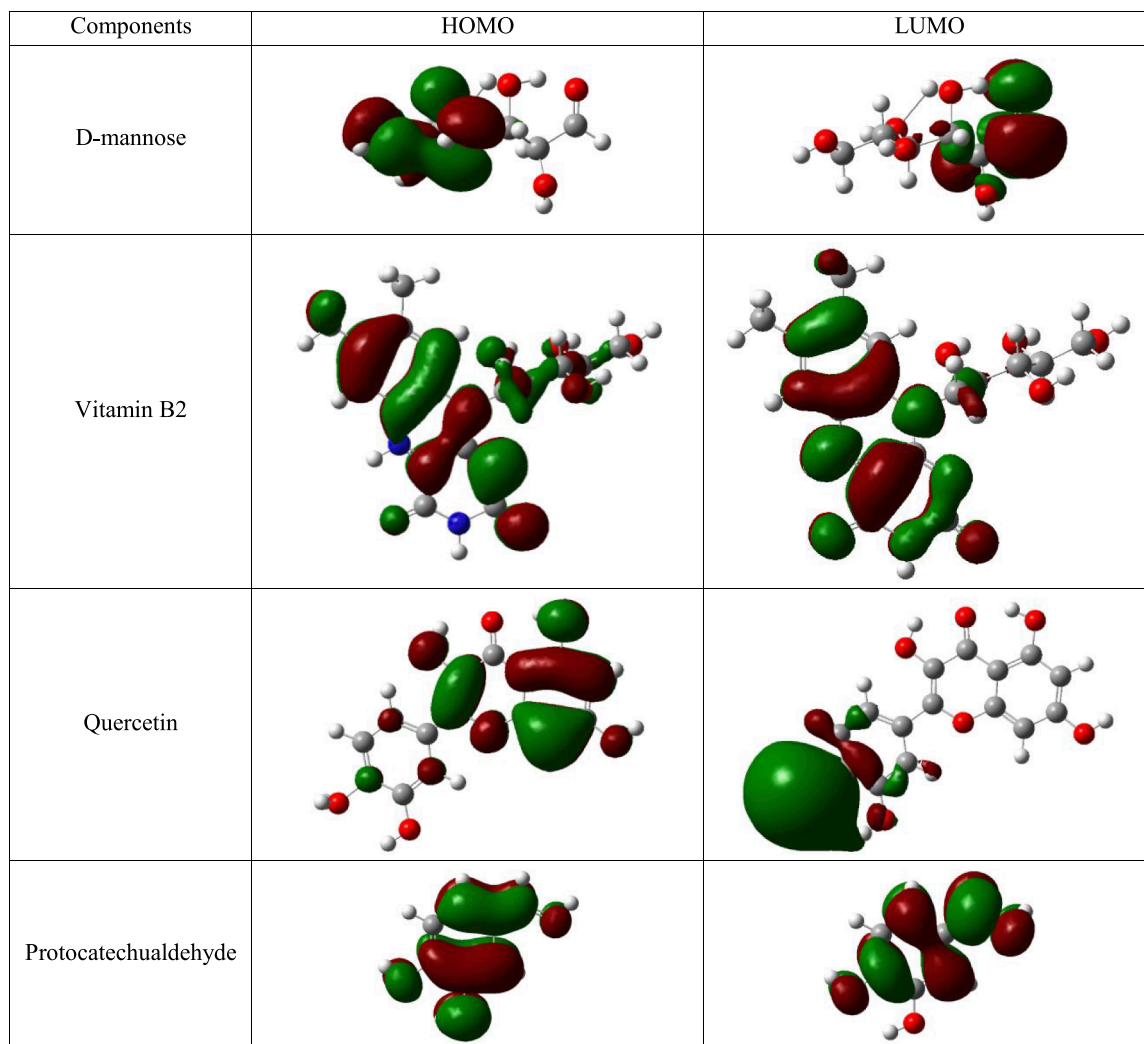


Fig. 18. Frontier molecular orbital distributions of the active components in IBLE in the protonated state.

Table 5

Energy activity parameters of four active components in IBLE based on DFT simulations.

Components	$E_{\text{HOMO}} / \text{eV}$	$E_{\text{LUMO}} / \text{eV}$	$\Delta E / \text{eV}$	I / eV	A / eV	χ / eV	ξ / eV	$\Delta N / \text{eV}$
Neutral form								
D-mannose	-7.15	-1.56	5.59	7.15	1.56	4.36	2.80	0.47
Vitamin B2	-6.26	-2.82	3.44	6.26	2.82	4.54	1.72	0.72
Quercetin	-5.72	-2.03	3.69	5.72	2.03	3.88	1.85	0.85
Protocatechualdehyde	-6.40	-1.68	4.72	6.40	1.68	4.04	2.36	0.63
Protonated form								
D-mannose	-11.21	-6.40	4.81	11.21	6.40	8.81	2.41	-0.38
Vitamin B2	-9.95	-7.46	2.49	9.95	7.46	8.71	1.25	-0.68
Quercetin	-8.53	-5.87	2.66	8.53	5.87	7.20	1.33	-0.08
Protocatechualdehyde	-10.78	-7.50	3.28	10.78	7.50	9.14	1.64	-0.65

rings, N-hybridized heterocycles, and carbonyls. Like D-mannose, vitamin B2 can act as an electron donor and acceptor in its neutral and protonated forms. The aromatic rings and carbonyls in vitamin B2 are the core components for chemical adsorption. Moreover, the polarity of vitamin B2 is extremely strong, with four hydroxyls, two carbonyls, and four N-hetero-atoms, which can also be physically adsorbed on the MS surface. It implies that the adsorption of vitamin B2 onto the MS surface is also achieved via multiple factors.

As shown in Figs. 17 and 18, the HOMO and LUMO distributions of quercetin and protocatechualdehyde in the neutral state cover almost the entire molecules. Protonation hardly changes the HOMO and LUMO

of protocatechualdehyde, but it significantly affects the distributions of quercetin. For the protonated quercetin, HOMO is primarily distributed on aromatic rings 1 and 2 and three connected hydroxyls, whereas LUMO is mainly located in protonated hydroxyl. The electron-donating and -receiving abilities, that is, the chemisorption capacity of quercetin after protonation, are reduced. However, protonation with positive charge and strong polarity guarantees the physical adsorption of quercetin onto the steel surface.

The larger the E_{HOMO} (Energy of the Highest Occupied Molecular Orbital), the stronger the ability of the molecule to donate electrons. Conversely, the smaller the E_{LUMO} (Energy of the Lowest Unoccupied

Molecular Orbital), the stronger the ability of the molecule to accept electrons (Musa et al., 2012). A smaller ΔE (the energy gap between E_{HOMO} and E_{LUMO}) indicates lower stability of the molecule and greater chemical reaction activity. As a result, coordination bonds between organic molecules and metal atoms can be generated more efficiently. The compounds formed this way are more stable and can improve corrosion inhibition (Wang et al., 2022).

As shown in Table 5, concerning four active components in the neutral state, the differences in E_{HOMO} is relatively small, and so is E_{LUMO} . However, E_{HOMO} of neutral quercetin is the highest, and E_{LUMO} of neutral vitamin B2 is the lowest. Therefore, ΔE of neutral quercetin and vitamin B2 is the smallest. The chemical reactions of neutral vitamin B2 and quercetin are the most active and can provide excellent corrosion inhibition for MS. ξ of neutral vitamin B2 and quercetin is also the softest. Ferrous ions in acidic solutions are soft (Rani et al., 2022). According to HSAB theory, the interaction of neutral vitamin B2 and quercetin with ferrous ions is a soft-soft reaction. The interaction products are stable. In addition, ΔN of four active components in the neutral form is smaller than 3.6 eV, further implying that these molecules have outstanding electron-donating and corrosion inhibition abilities (Rani et al., 2022). The electron-donating abilities enhance with an increase in ΔN . ΔN of neutral vitamin B2 and quercetin is the highest, followed by neutral protocatechualdehyde, while that of neutral D-mannose is the smallest.

The energy activity parameters of the organic molecules in the neutral and protonated states were also compared. After protonation, E_{HOMO} and E_{LUMO} of four active components decrease. It suggests a decrease in electron-donating ability but an enhancement in electron-receiving ability. Because the drop degree of E_{LUMO} is more evident than that of E_{HOMO} , ΔE is also decreased, resulting in lower stability, greater reactivity, and better corrosion inhibition. The decrease in ξ also infers the stability improvement of the interaction products between organic molecules and ferrous ions. Moreover, ΔN of four components after protonation is negative, demonstrating an excellent ability to receive electrons from the 3d orbits of iron. Combined with Lukovit's theory, four protonated molecules can not only donate electrons (such as lone pair electrons, π electrons) to the 3d empty orbits of iron but also receive electrons from the filled 3d orbits (Rani et al., 2022). After protonation, four active molecules exhibit an outstanding synergistic adsorption effect on electron-providing and -receiving. Therefore, they can provide positive corrosion inhibition for MS.

A longitudinal comparison of the energy activity parameters of four protonated molecules was also performed. ΔE of protonated vitamin B2 and quercetin is the minimum, followed by protonated protocatechualdehyde and D-mannose. The sequencing law of ξ of four protonated molecules is similar to that of ΔE . The corrosion protection efficiency provided by protonated vitamin B2 and quercetin is the highest, whereas that of protonated D-mannose is relatively minimal. This is consistent with the observations in the neutral state.

The above results based on energy activity parameters demonstrate that the adsorption ability of neutral and protonated vitamin B2 and quercetin among four organic molecules is the strongest, as is the corrosion inhibition efficiency. It can be attributed to more aromatic rings, heterocycles, and hetero-atoms in vitamin B2 and quercetin, which have more lone pair electrons and π electrons. It can be confirmed by the difference in ΔN . ΔN of the protonated vitamin B2 and protocatechualdehyde is the most negative, followed by the protonated D-mannose. The largest ΔN of the protonated quercetin occurs because its LUMO is mainly located at the protonated hydroxy, of which the LUMO volume is the smallest (Fig. 18). However, LUMO of the protonated vitamin B2 and protocatechualdehyde are distributed in aromatic rings. Therefore, the corrosion inhibition of quercetin is mainly due to the electron donor, while that of vitamin B2, protocatechualdehyde, and D-mannose occurs through a synergistic mechanism involving both electron donors and electron acceptors. The electron-donating and -receiving capacities depend on the HOMO and LUMO distributions,

which are directly related to the number of aromatic rings, heterocycles, and hetero-atoms in organic molecules.

4.6. MD calculation results

To further explain the corrosion inhibition mechanism of IBLE, the adsorption pattern and the coverage efficiency of the active molecules on the MS surface were investigated via MD simulations. The corresponding energy was calculated as follows (Attou et al., 2020; Bahlakeh et al., 2019):

$$E_{\text{ads}} = E_{\text{inter}} = E_{\text{tot}} - (E_{\text{steel+sol}} + E_{\text{inh}}) \quad (19)$$

$$E_{\text{binding}} = -E_{\text{ads}} \quad (20)$$

where E_{ads} is the adsorption energy of the inhibitor molecules on the MS surface, E_{tot} is the energy of the entire system containing the inhibitor molecules, water molecules, and iron atoms, $E_{\text{steel+sol}}$ is the system energy of the iron atoms and water molecules, E_{inh} is the energy of the inhibitor molecules, E_{binding} is the binding energy of the inhibitor molecules on the Fe(110) surface, E_{inter} is the interaction energy between the inhibitor molecules and the MS surface. For the adsorption system in this study, E_{ads} and E_{inter} were equal.

The side and top views of the final stable configurations of four active components adsorbed on the Fe (110) plane based on MD simulations are shown in Figs. 19 and 20. The corresponding E_{ads} is listed in Table 6.

In general, molecules adsorbed in a pattern parallel to the metal surface can provide greater coverage and more consistency of the protective film, strengthening the mechanical barrier function and providing a better protection effect (Abdellattif et al., 2021; Zhang et al., 2022). As shown in Figs. 19 and 20, four components of D-mannose, vitamin B2, quercetin, and protocatechualdehyde in IBLE, in both the neutral and protonated states, are almost adsorbed in parallel on the surface of Fe (110). They can be used as effective corrosion inhibitors for MS. Moreover, the geometric configurations of vitamin B2 and quercetin, with three aromatic rings and multiple hetero-atoms, are larger, as are their surface coverage and corrosion inhibition. As mentioned in the DFT simulations, the neutral and protonated vitamin B2 and quercetin molecules can interact with iron atoms more easily than the other two molecules. It further verifies the corrosion mechanism of the geometric coverage effect deduced from the electrochemical tests.

The stable configuration snapshots based on MD simulations and the HOMO and LUMO distributions based on DFT simulations were compared in detail, revealing differences between D-mannose and quercetin. For the protonated quercetin, the entire molecule is almost completely adsorbed on the Fe (110) surface in parallel, but LUMO and HOMO are only distributed on some atoms. Similar differences were observed for the protonated D-mannose. These phenomena further indicate that the physical adsorption of the protonated quercetin and D-mannose, due to electrostatic attraction, dispersive force, and induced force, is extremely strong and may even be greater than the chemical adsorption effect. This is in good agreement with the ΔG_{ads} results, where the adsorption of active components in IBLE is mixed adsorption, slightly dominated by physical adsorption.

As shown in Table 6, E_{ads} of four active components in both neutral and protonated forms are negative, further suggesting a spontaneous adsorption process. E_{ads} in the protonated form are lower than those in the neutral form. After protonation, E_{ads} of quercetin, D-mannose, vitamin B2, and protocatechualdehyde decrease by approximately 40.8 %, 27.5 %, 12.0 %, and 14.4 %, respectively. The decrease in the former two is far greater than that of the latter two, indicating a greater enhancement in spontaneous adsorption tendency and physical adsorption of quercetin and D-mannose after protonation. Moreover, E_{ads} of vitamin B2 and quercetin is significantly lower than that of the other two molecules. The stronger tendency of spontaneous adsorption

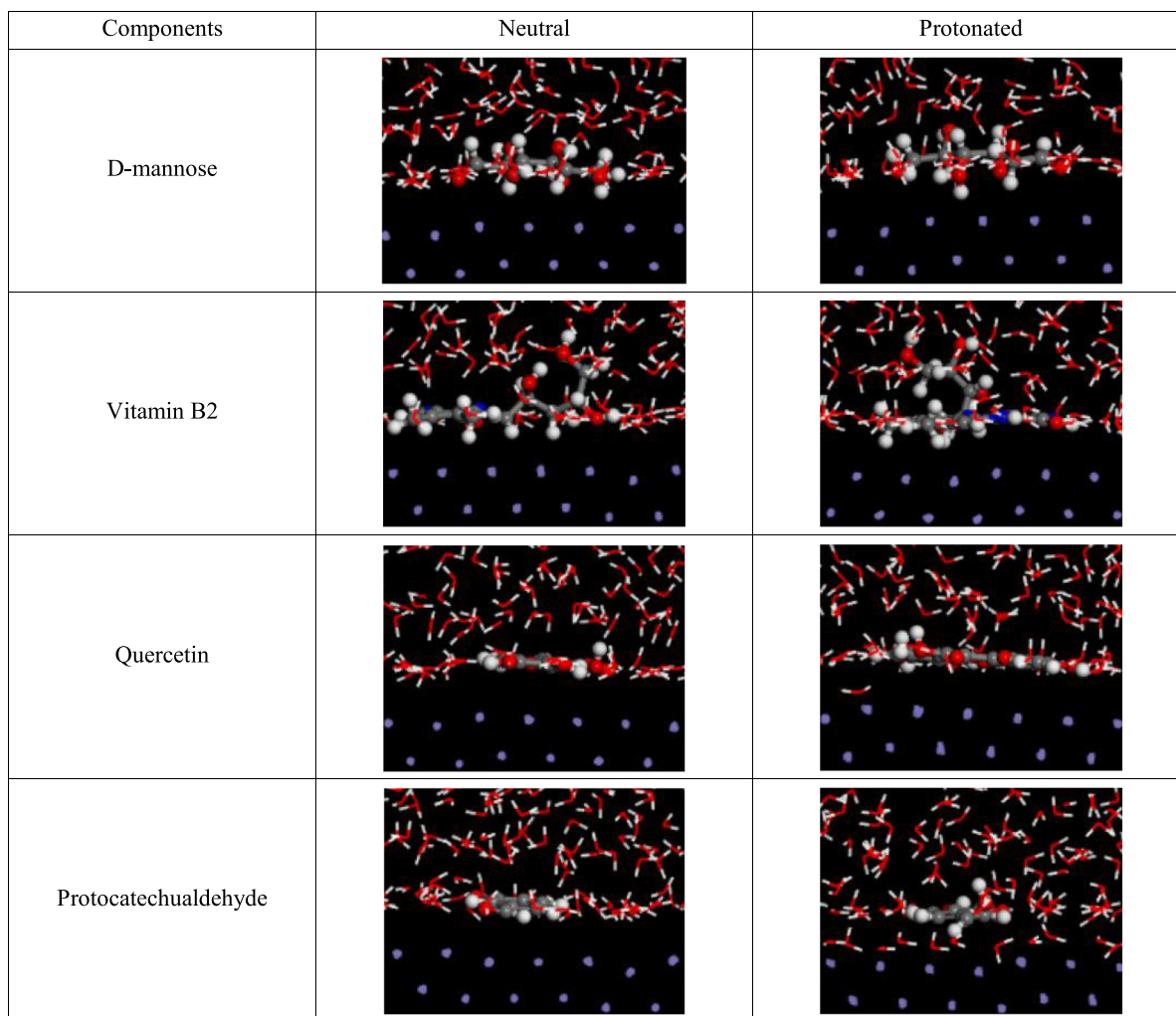


Fig. 19. Side view of the final snapshots of active components on the surface of Fe (110) based on MD simulations.

is related to more aromatic rings and hetero-atoms.

With greater E_{binding} , the binding force between the organic molecules and the metal surface is stronger, as is the ability of the organic molecules to replace the initially adsorbed chloride ions and water molecules. A larger E_{binding} suggests that the formed adsorption film is firmer and can improve corrosion protection performance. This study focuses on the adsorption system of organic molecules on the steel surface; therefore, E_{binding} is the opposite of E_{ads} . According to E_{ads} in Table 6, E_{binding} of four active components after protonation is prominently enhanced, and E_{binding} of vitamin B2 and quercetin is approximately two to three times greater than that of D-mannose and protocatechualdehyde. It additionally demonstrates that vitamins B2 and quercetin in IBLE can offer better inhibition properties for MS. Notably, the components of IBLE are very complex, and besides these four representatives, other compounds synergistically exert adsorption and corrosion inhibition functions.

4.7. Adsorption and inhibition mechanism

The corrosion inhibition performance of organic molecules mainly depends on the adsorption capacity on the metal surface, which is closely related to the molecular structure. The HOMO and LUMO distributions and the numbers of π and lone pair electrons directly depend on the numbers of aromatic rings, hetero-atoms, carbonyls and hydroxyls, and the chemical reaction activity of the interaction between organic molecules and metal atoms/ions are thus determined. The

ability of organic molecules to donate electrons to the unfilled orbitals and receive electrons from the filled orbitals of metals was ascertained. The greater the number of aromatic rings, hetero-atoms, carbonyls, and hydroxyls, the lower the chemical stability and the easier the chemical reaction between organic molecules and metals. The synergistic adsorption effect of electron donation and reception is more significant, making it easier to replace the active chloride ions and water molecules that were initially adsorbed on the metal surface. The global hardness of organic molecules in IBLE is soft, so the stability of the reaction products with iron ions in acidic media is strong. In addition, polar groups such as carbonyls, hydroxyls, ketones, and hetero-atoms enhance physical adsorption. After the protonation of organic molecules in acidic media, the spontaneous adsorption tendency and physical adsorption were further strengthened. The electron donor and acceptor thus have a synergistic adsorption effect. Moreover, a strong electrostatic attraction between the positively charged protonated molecules and the active chloride ions, which were adsorbed initially on the metal surface, generates physical adsorption (Abdellattif et al., 2019). D-mannose in IBLE has no aromatic ring, but the strong polar carbonyl and hydroxyl groups ensure that it still exhibits a relatively strong mixed adsorption capacity of physical and chemical adsorption. Vitamin B2, quercetin, and protocatechualdehyde in IBLE have aromatic rings, carbonyls, and hydroxyls, of which there are up to three aromatic rings in vitamin B2 and quercetin. This results in an excellent mixed adsorption effect and high coverage of adsorption film. In addition, as the active ingredients in IBLE adsorb onto the surface, the surface active area of MS decreases. Close to

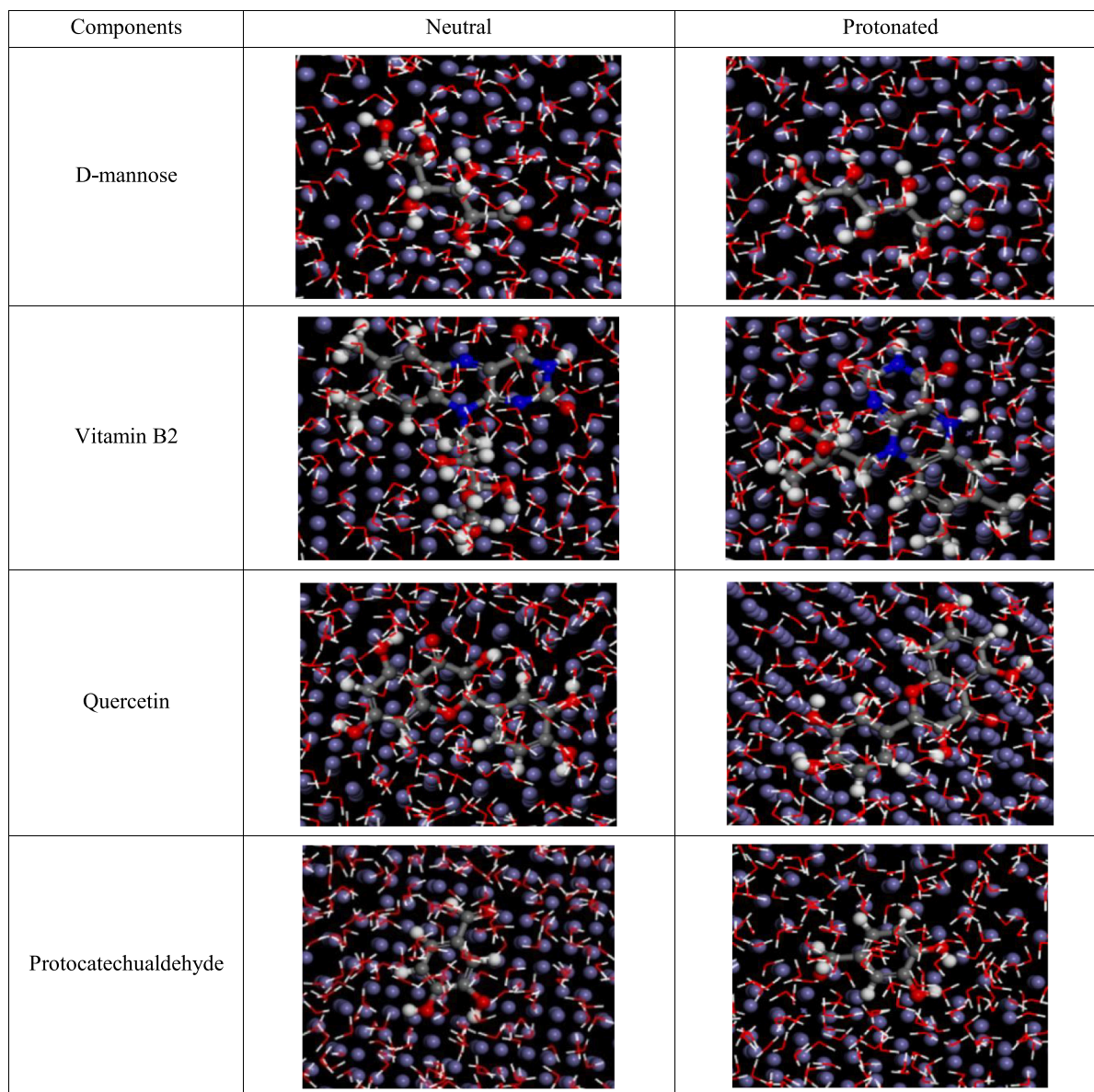


Fig. 20. Top view of the final snapshots of active components on the surface of Fe (110) based on MD simulations.

Table 6

E_{ads} of four active components in IBLE adsorbed on the Fe (110) surface based on MD simulations (kcal/mol).

Molecules	Neutral form	Protonated form
D-mannose	-80.3	-102.4
Vitamin B2	-270.2	-302.5
Quercetin	-220.6	-310.6
Protocatechualdehyde	-105.7	-120.9

the IBLE-covered surface, Fe^{2+} is further oxidized to Fe^{3+} , while the cathodic hydrogen evolution reaction leads to an increase in pH at the local sites. The combined effect of these two reactions is beneficial for the formation of trivalent iron oxides/hydroxides, improving the density and coverage of the corrosion product film, thereby further enhancing the corrosion resistance of MS. The components in IBLE are highly complex, which, in turn, provide mutually optimized adsorption behaviours. The adsorption film can effectively block the contact between the metal and corrosive medium and inhibit the corrosion of the covered metal surface. By contrast, the original corrosion reactions in acidic

media still occur on the uncovered surface. Therefore, IBLE is an excellent corrosion inhibitor for MS in 1 M HCl solution and can provide a corrosion inhibition mechanism of geometric coverage effect. Taking vitamin B2 as an example, a schematic of the adsorption and inhibition mechanisms of the active components in IBLE on the MS surface is shown in Fig. 21.

5. Conclusions

Ipomoea batatas L. leaves, which are abundant agricultural by-products, contain many active phytochemicals such as amino acids, vitamins, sugars, flavonoids, and phenolic acids. From an environmental protection perspective, an ultrasonic-assisted method was used to prepare the ethanol-water extract from *Ipomoea batatas L.* leaves. This extract (IBLE) was attempted as an eco-friendly corrosion inhibitor for MS in a 1 M HCl pickling solution. The corrosion inhibition and adsorption mechanisms of the active components in IBLE were studied experimentally and theoretically. The main conclusions are as follows:

IBLE is an excellent mixed corrosion inhibitor for MS. The inhibition efficiency is enhanced by increasing the extract concentration and

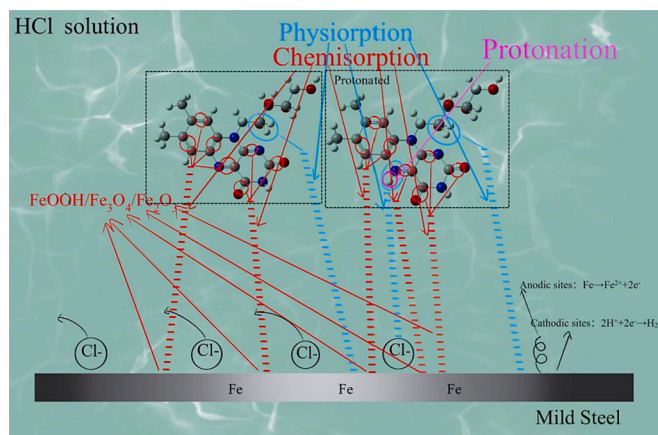


Fig. 21. Schematic diagram of the adsorption and inhibition of the active ingredients on the MS surface in HCl solution (Taken vitamin B2 as an example).

solution temperature. With 5.0 g/L IBLE, the inhibition efficiencies at 298, 308, and 318 K are 94.9 %, 95.6 %, and 96.6 %, respectively. The inhibition mechanism is the geometric coverage effect. The PDP and EIS tests do not affect the evaluation of the adsorption isotherms and thermodynamics parameters of the active components in IBLE onto the MS surface. The adsorption of organic molecules follows the Langmuir isotherm, which is the mixed adsorption with a slight dominance by physical adsorption. XPS confirms that the active components, including the protonated form, participate in the formation of the adsorption film. SEM observations verify the significant inhibitory effect of IBLE on MS corrosion. IBLE can be used as an efficient and renewable corrosion inhibitor for MS in an HCl pickling solution.

In IBLE, D-mannose, vitamin B2, quercetin, and protocatechualdehyde were selected to represent sugars, vitamins, flavonoids, and phenolic acids to display the theoretical simulation results. DFT simulations show that the HOMO and LUMO distributions of active components in IBLE exhibit the outstanding ability to provide π and/or lone pair electrons to the unfilled 3d orbits of iron atoms and to receive electrons from the outer filled orbits of iron atoms. The active molecules possess a synergistic adsorption effect, which is enhanced after protonation. The coordination bonds and chemical adsorption are generated between the organic molecules and iron atoms, forming the stable coordination compounds on the MS surface. Based on MD simulations, the active components in IBLE are adsorbed on the Fe (110) surface in parallel, and a significant physical adsorption effect is proved. The adsorption capacity of organic molecules is closely related to the number and type of aromatic rings, hetero-atoms, and polar groups.

Declaration of Competing Interest

The authors declare that they have no known competing financial interests or personal relationships that could have appeared to influence the work reported in this paper.

Acknowledgements

This work was supported by the National Natural Science Foundation of China (No. 52178484), the Natural Science Foundation of Fujian Province (Nos. 2020J01291 and 2020J01059), and the “Scientific Research Climbing Plan” of Xiamen University of Technology (No. XPKDT20002), and the Xiamen Construction Science and Technology Plan Project (No. XJK2022-1-2).

References

Abdellattif, M., Alrefaee, S., Dagdag, O., Verma, C., Quraishi, M.A., 2021. *Calotropis procera* extract as an environmental friendly corrosion inhibitor: Computational

demonstrations. *J. Mol. Liq.* 337, 116954 <https://doi.org/10.1016/j.molliq.2021.116954>.

- Ahmed, R., Zhang, S., 2020. Bee pollen extract as an eco-friendly corrosion inhibitor for pure copper in hydrochloric acid. *J. Mol. Liq.* 316, 113849 <https://doi.org/10.1016/j.molliq.2020.113849>.
- Alibakhshi, E., Ramezanzadeh, M., Bahlakeh, G., Ramezanzadeh, B., Mahdavian, M., Motamedi, M., 2018. *Glycyrrhiza glabra* leaves extract as a green corrosion inhibitor for mild steel in 1 M hydrochloric acid solution: Experimental, molecular dynamics, Monte Carlo and quantum mechanics study. *J. Mol. Liq.* 255, 185–198. <https://doi.org/10.1016/j.molliq.2018.01.144>.
- Aljourani, J., Raeissi, K., Golozar, M., 2009. Benzimidazole and its derivatives as corrosion inhibitors for mild steel in 1 M HCl solution. *Corros. Sci.* 51, 1836–1843. <https://doi.org/10.1016/j.corsci.2009.05.011>.
- Alrebh, A., Rammal, M., Omanovic, S., 2021. A pyridine derivative 2-(2-Methylaminoethyl)pyridine (MAEP) as a ‘green’ corrosion inhibitor for low-carbon steel in hydrochloric acid media. *J. Mol. Struct.* 1238, 130333 <https://doi.org/10.1016/j.molstruc.2021.130333>.
- AlSalhi, M.S., Devanesan, S., Rajasekar, A., Kokilaramani, S., 2023. Characterization of plants and seaweeds based corrosion inhibitors against microbially influenced corrosion in a cooling tower water environment. *Arab. J. Chem.* 16, 104513 <https://doi.org/10.1016/j.arabjc.2022.104513>.
- Asadi, N., Ramezanzadeh, M., Bahlakeh, G., Ramezanzadeh, B., 2019. Utilizing *Lemon balm* extract as an effective green corrosion inhibitor for mild steel in 1 M HCl solution: A detailed experimental, molecular dynamics, Monte Carlo and quantum mechanics study. *J. Taiwan Inst. Chem. Eng.* 95, 252–272. <https://doi.org/10.1016/j.jtice.2018.07.011>.
- Asfia, M., Rezaei, M., 2021. A study on localized corrosion behavior of 304 stainless steel in the presence of *Allium sativum* extract inhibitor using electrochemical noise analysis. *Mater. Chem. Phys.* 274, 125158 <https://doi.org/10.1016/j.matchemphys.2021.125158>.
- Attou, A., Tourabi, M., Benikdes, A., Benali, O., Ouicf, H., Benhiba, F., Zarrouk, A., Jama, C., Bentiss, F., 2020. Experimental studies and computational exploration on the 2-amino-5-(2-methoxyphenyl)-1,3,4-thiadiazole as novel corrosion inhibitor for mild steel in acidic environment. *Colloids Surf. A Physicochem. Eng. Asp.* 604, 125320 <https://doi.org/10.1016/j.colsurfa.2020.125320>.
- Azzouzi, M., Azzaoui, K., Warad, I., Hammouti, B., Shiyakov, S., Sabbahi, R., Saoiabi, S., Youssoufi, M., Akartasse, N., Jodeh, S., 2022. *Moroccan, Mauritania*, and senegalese gum *Arabic variants* as green corrosion inhibitors for mild steel in HCl: Weight loss, electrochemical, AFM and XPS studies. *J. Mol. Liq.* 347, 118354 <https://doi.org/10.1016/j.molliq.2021.118354>.
- Bahlakeh, G., Dehghani, A., Ramezanzadeh, B., Ramezanzadeh, M., 2019. Highly effective mild steel corrosion inhibition in 1 M HCl solution by novel green aqueous *Mustard* seed extract: Experimental, electronic-scale DFT and atomic-scale MC/MD explorations. *J. Mol. Liq.* 293, 111559 <https://doi.org/10.1016/j.molliq.2019.111559>.
- Benghalia, M., Fares, C., Khadraoui, A., Meliani, M., Obot, I., Sorrou, A., Dmytrakh, M., Azari, Z., 2018. Performance evaluation of a natural and synthetic compound as corrosion inhibitors of API 5L X52 steel in hydrochloric acid media. *Mor. J. Chem.* 6, 6–61. <https://doi.org/10.48317/IMIST.PRSM/morjchem-v6i1.8608>.
- Berdimurodov, E., Kholikov, A., Akbarov, K., Guo, L., Abdullah, A., Elik, M., 2021. A gossypol derivative as an efficient corrosion inhibitor for St2 steel in 1 M HCl + 1 M KCl: An experimental and theoretical investigation. *J. Mol. Liq.* 328, 115475 <https://doi.org/10.1016/j.molliq.2021.115475>.
- Berrissoul, A., Ouarhach, A., Benhiba, F., Romane, A., Guenbour, A., Dikici, B., Bentiss, F., Zarrouk, A., Dafali, A., 2022. Assessment of corrosion inhibition performance of *Origanum compactum* extract for mild steel in 1 M HCl: Weight loss, electrochemical, SEM/EDX, XPS, DFT and molecular dynamic simulation. *Ind. Crop. Prod.* 187, 115310 <https://doi.org/10.1016/j.indcrop.2022.115310>.
- Bhardwaj, N., Sharma, P., Kumar, V., 2021. *Triticum aestivum* extract as corrosion inhibitor for stainless steel (SS-410) in acidic media: Experimental and theoretical study. *Curr. Opin. Green. Sustain. Chem.* 4, 100189 <https://doi.org/10.1016/j.crgsc.2021.100189>.
- Bhardwaj, N., Sharma, P., Guo, L., Dagdag, O., Kumar, V., 2022. Molecular dynamic simulation, quantum chemical calculation and electrochemical behaviour of *Punica granatum* peel extract as eco-friendly corrosion inhibitor for stainless steel (SS-410) in acidic medium. *J. Mol. Liq.* 346, 118237 <https://doi.org/10.1016/j.molliq.2021.118237>.
- Bidi, M., Azadi, M., Rassouli, M., 2021. An enhancement on corrosion resistance of low carbon steel by a novel bio-inhibitor (*Leech* extract) in the H₂SO₄ solution. *Surf. Interfaces* 24, 101159. <https://doi.org/10.1016/j.surfin.2021.101159>.
- Bouanis, M., Tourabi, M., Nyassi, A., Zarrouk, A., Jama, C., Bentiss, F., 2016. Corrosion inhibition performance of 2,5-bis (4-dimethylaminophenyl)-1,3,4-oxadiazole for carbon steel in HCl solution: Gravimetric, electrochemical and XPS studies. *Appl. Surf. Sci.* 389, 952–966. <https://doi.org/10.1016/j.apsusc.2016.07.115>.
- Chen, S., Chen, S., Zhu, B., Huang, C., Li, W., 2020. *Magnolia grandiflora* leaves extract as a novel environmentally friendly inhibitor for Q235 steel corrosion in 1 M HCl: Combining experimental and theoretical researches. *J. Mol. Liq.* 311, 113312 <https://doi.org/10.1016/j.molliq.2020.113312>.
- Chen, J., Wu, Y., Guo, L., Li, W., Tan, B., Brahmia, A., 2023. Insight into the anti-corrosion mechanism of *Pisum sativum L* leaves extract as the degradable inhibitor for Q235 steel in sulfuric acid medium. *J. Taiwan Inst. Chem. Eng.* 143, 104664 <https://doi.org/10.1016/j.jtice.2022.104664>.
- Chrysochoou, M., Oakes, J., Dyar, M., 2018. Investigation of iron reduction by green tea polyphenols. *Appl. Geochem.* 97, 163–269. <https://doi.org/10.1016/j.apgeochem.2018.08.026>.

- Dehghani, A., Bahlakeh, G., Ramezanzadeh, B., Ramezanzadeh, M., 2019a. A combined experimental and theoretical study of green corrosion inhibition of mild steel in HCl solution by aqueous *Citrullus lanatus* fruit (CLF) extract. *J. Mol. Liq.* 279, 603–624. <https://doi.org/10.1016/j.molliq.2019.02.010>.
- Dehghani, A., Bahlakeh, G., Ramezanzadeh, B., Ramezanzadeh, M., 2019b. Potential of *Borage* flower aqueous extract as an environmentally sustainable corrosion inhibitor for acid corrosion of mild steel: Electrochemical and theoretical studies. *J. Mol. Liq.* 277, 895–911. <https://doi.org/10.1016/j.molliq.2019.01.008>.
- Dewangan, Y., Verma, D.K., Berdimurodov, E., Haldhar, R., Dagdag, O., Tripathi, M., 2022. N-hydroxypyrazine-2-carboxamide as a new and green corrosion inhibitor for mild steel in acidic medium: experimental, surface morphological and theoretical approach. *J. Adhes. Sci. Technol.* 36 (23–24), 2644–2664. <https://doi.org/10.1080/01694243.2022.2068884>.
- Eid, A.M., Shaaban, S., Shalabi, K., 2020. Tetrazole-based organoselenium bi-functionalized corrosion inhibitors during oil well acidizing: Experimental, computational studies, and SRB bioassay. *J. Mol. Liq.* 298, 111980. <https://doi.org/10.1016/j.molliq.2019.11.1980>.
- El-Asri, A., Rguiti, M.M., Jmiai, A., Oukhrib, R., Bourzi, H., Lin, Y., Issami, S.E., 2022. *Carissa macrocarpa* extract (ECM) as a new efficient and ecologically friendly corrosion inhibitor for copper in nitric acid: Experimental and theoretical approach. *J. Taiwan Inst. Chem. Eng.* 142, 104633. <https://doi.org/10.1016/j.jtice.2022.104633>.
- El-Hashemy, M., Sallam, A., 2020. The inhibitive action of *Calendula officinalis* flower heads extract for mild steel corrosion in 1 M HCl solution. *J. Master Res. Technol.* 9, 13509–13523. <https://doi.org/10.1016/j.jmrt.2020.09.078>.
- Fernandes, C., Fagundes, T., Nazir, E., Talita, S., Garrett, R., Borges, R., Muricy, G., Valverde, A., Ponzio, E., 2019. *Ircinia strobilina* crude extract as corrosion inhibitor for mild steel in acid medium. *Electrochim. Acta* 312, 137–148. <https://doi.org/10.1016/j.electacta.2019.04.148>.
- Fernie, Y., Ech-chihbi, E., Arrousse, N., Hajjaji, F.E., Bousraf, F., Touhami, M.E., Rais, Z., Taleb, M., 2021. Ocimum basilicum seeds extract as an environmentally friendly antioxidant and corrosion inhibitor for aluminium alloy 2024-T3 corrosion in 3 wt% NaCl medium. *Colloids Surf.* 627, 127232. <https://doi.org/10.1016/j.colsurfa.2021.127232>.
- Hashim, N., Anouar, E., Kassim, K., Zaki, H., Alharthi, A., Embong, Z., 2019. XPS and DFT investigations of corrosion inhibition of substituted benzylidene Schiff bases on mild steel in hydrochloric acid. *Appl. Surf. Sci.* 476, 861–877. <https://doi.org/10.1016/j.apsusc.2019.01.149>.
- Hemapriya, V., Prabakaran, M., Chitra, S., Swathika, M., Kim, S.H., Chung, I.M., 2020. Utilization of biowaste as an eco-friendly biodegradable corrosion inhibitor for mild steel in 1 mol/L HCl solution. *Arab. J. Chem.* 13, 8684–8696. <https://doi.org/10.1016/j.arabj.2020.09.060>.
- Hsu, C.H., Mansfeld, F., 2001. Concerning the conversion of the constant phase element parameter Y_0 into a capacitance. *Corrosion* 57, 747–748. <https://doi.org/10.5006/1.3280607>.
- Hu, Y., Fan, B., Liu, H., Fan, F., Hao, H., Yang, B., 2020. Mechanism of corrosion inhibition of copper in sulfuric acid solution by *Durian* flesh peel/core extract. *Corros. Prot.* 41, 17–24.
- Hu, J., Xiong, Q., Chen, L., Zhang, C., Zheng, Z., Geng, S., Yang, Z., Zhong, X., 2021. Corrosion inhibitor in CO₂-O₂-containing environment: Inhibition effect and mechanisms of Bis (2-ethylhexyl) phosphate for the corrosion of carbon steel. *Corros. Sci.* 179, 109173. <https://doi.org/10.1016/j.corsci.2020.109173>.
- Itoen, E., Akaranta, O., James, A., Sun, S., 2017. Green and sustainable local biomaterials for oilfield chemicals: *Griffonia simplicifolia* extract as steel corrosion inhibitor in hydrochloric acid. *Sustain. Mater. Technol.* 11, 2–18. <https://doi.org/10.1016/j.susmat.2016.12.001>.
- Kalyn, T., Poberezhny, L., Popovych, P., Rudiak, Y., Korol, O., Poberezhna, L., 2022. Evaluation of the green inhibitor effect on the corrosion of pipeline steel in N54 medium. *Procedia Struct. Integr.* 36, 313–317. <https://doi.org/10.1016/j.prostr.2022.01.040>.
- Karki, N., Neupane, S., Gupta, D.K., Das, D.K., Singh, S., Koju, G.M., Chaudhary, Y., Yadav, A.P., 2021. *Berberine* isolated from *Mahonia nepalensis* as an eco-friendly and thermally stable corrosion inhibitor for mild steel in acid medium. *Arab. J. Chem.* 14, 103423. <https://doi.org/10.1016/j.arabj.2021.103423>.
- Kathiravan, S., Jyothi, S., Ayyannan, G., Ravichandran, J., Raja, G., 2021. Inhibitory action of aqueous *Ruellia tuberosa* L. leaves extract on the corrosion of copper in HCl solution. *J. Indian Chem. Soc.* 98, 100207. <https://doi.org/10.1016/j.jics.2021.100207>.
- Khadom, A., Kadhim, M., Anae, R., Mahood, H., Mahdi, M., Salamm, A., 2021. Theoretical evaluation of *Citrus Aurantium* leaf extract as green inhibitor for chemical and biological corrosion of mild steel in acidic solution: Statistical, molecular dynamics, docking, and quantum mechanics study. *J. Mol. Liq.* 343, 116978. <https://doi.org/10.1016/j.molliq.2021.116978>.
- Khadraoui, A., Khelifa, A., Hachama, K., Mehdaoui, R., 2016. *Thymus algeriensis* extract as a new eco-friendly corrosion inhibitor for 2024 aluminium alloy in 1M HCl medium. *J. Mol. Liq.* 214, 293–297. <https://doi.org/10.1016/j.molliq.2015.12.064>.
- Khayatkashani, M., Soltani, N., Tavakkoli, N., Nejatian, A., Ebrahimi, J., Mahdi, M., Salavati-Niasari, M., 2022. Insight into the corrosion inhibition of *Biebersteinia multifida* root extract for carbon steel in acidic medium. *Sci. Total Environ.* 836, 155527. <https://doi.org/10.1016/j.scitotenv.2022.155527>.
- Kusumaningrum, L., Soenoko, R., Siswanto, E., Gapsari, F., 2022. Investigation of *Artocarpus heterophyllus* peel extract as non-toxic corrosion inhibitor for pure copper protection in nitric acid. *Case Stud. Chem. Environ. Eng.* 6, 100223. <https://doi.org/10.1016/j.csee.2022.100223>.
- Li, F., Bai, M., Wei, S., Jin, S., Shen, W., 2019. Multidimension insight involving experimental and in silico investigation into the corrosion inhibition of N, N-dibenzyl dithiocarbamate acid on copper in sulfuric acid solution. *Ind. Eng. Chem. Res.* 58, 7166–7178. <https://doi.org/10.1021/acs.iecr.9b00371>.
- Li, H., Qiang, Y., Zhao, W., Zhang, S., 2021. A green *Brassica oleracea* L extract as a novel corrosion inhibitor for Q235 steel in two typical acid media. *Colloids Surf. A Physicochem. Eng. Asp.* 616, 126077. <https://doi.org/10.1016/j.colsurfa.2020.126077>.
- Liao, B., Luo, Z., Wan, S., Chen, L., 2023. Insight into the anti-corrosion performance of *Acanthopanax senticosus* leaf extract as eco-friendly corrosion inhibitor for carbon steel in acidic medium. *J. Ind. Eng. Chem.* 117, 238–246. <https://doi.org/10.1016/j.jiec.2022.10.010>.
- Liao, L., Mo, S., Luo, H., Li, N., 2017. *Longan seed* and peel as environmentally friendly corrosion inhibitor for mild steel in acid solution: Experimental and theoretical studies. *J. Colloid Interface Sci.* 499, 110–119. <https://doi.org/10.1016/j.jcis.2017.03.091>.
- Lin, B., Shao, J., Xu, Y., Lai, Y., Zhao, Z., 2021. Adsorption and corrosion of renewable inhibitor of *Pomelo peel* extract for mild steel in phosphoric acid solution. *Arab. J. Chem.* 14 (5), 103114. <https://doi.org/10.1016/j.arabj.2021.103114>.
- Lin, B., Shao, J., Zhao, C., Zhou, X., He, F., Xu, Y., 2023. *Passiflora edulis Sims* peel extract as a renewable corrosion inhibitor for mild steel in phosphoric acid solution. *J. Mol. Liq.* 375, 121296. <https://doi.org/10.1016/j.molliq.2023.121296>.
- Liu, X., Gao, Y., Guan, J., Zhang, Q., Lin, Y., Shi, C., Wang, Y., Du, J., Ma, N., 2023. Corrosion inhibition properties of spinach extract on Q235 steel in a hydrochloric acid medium. *Arab. J. Chem.* 16, 105066. <https://doi.org/10.1016/j.arabj.2023.105066>.
- Luo, D., Mu, T., Sun, H., 2021. Profiling of phenolic acids and flavonoids in sweet potato (*Ipomoea batatas* L.) leaves and evaluation of their anti-oxidant and hypoglycemic activities. *Food Biosci.* 39, 100801. <https://doi.org/10.1016/j.fbio.2020.100801>.
- Mansfeld, F., 2005. Tafel slopes and corrosion rates obtained in the pre-Tafel region of polarization curves. *Corros. Sci.* 47, 3178–3186. <https://doi.org/10.1016/j.corsci.2005.04.012>.
- Mostafatabar, B., Dehghani, A., Ghahremani, P., Bahlakeh, G., Ramezanzadeh, B., 2022. Molecular-dynamic/DFT-electronic theoretical studies coupled with electrochemical investigations for analyzing the carrot pomace extract-based molecules inhibiting potency toward mild steel corrosion in 1 M HCl solution. *J. Mol. Liq.* 346, 118344. <https://doi.org/10.1016/j.molliq.2021.118344>.
- Mourya, P., Banerjee, S., Singh, M., 2014. Corrosion inhibition of mild steel in acidic solution by *Tagetes erecta* (Marigold flower) extract as a green inhibitor. *Corros. Sci.* 85, 352–363. <https://doi.org/10.1016/j.corsci.2014.04.036>.
- Mukhopadhyay, S., Dasgupta, S., Roy, S., Mondal, A., Sukul, D., Ghosal, S., Adhikari, U., 2021. Corrosion inhibition of mild steel by aqueous leaf extract of *Purple hedge* plant: Experimental and theoretical investigation. *J. Bio-Tribo-Corros.* 7, 1–20. <https://doi.org/10.1007/s40735-021-00577-6>.
- Musa, A., Jalgham, R., Mohamad, A., 2012. Molecular dynamic and quantum chemical calculations for phthalazine derivatives as corrosion inhibitors of mild steel in 1M HCl. *Corros. Sci.* 56, 176–183. <https://doi.org/10.1016/j.corsci.2011.12.005>.
- Nikpour, S., Karati, M., Bahlakeh, G., Ramezanzadeh, B., Mahdavian, M., 2019. *Eriobotrya japonica Lindl* leaves extract application for effective corrosion mitigation of mild steel in HCl solution: Experimental and computational studies. *Constr. Build. Mater.* 220, 161–176. <https://doi.org/10.1016/j.conbuildmat.2019.06.005>.
- Oliveiras-Xometel, O., Likhanova, N., Dominguez-Aguilar, M., Hallen, J., Zamudio, L., Arce, E., 2006. Surface analysis of inhibitor films formed by imidazolines and amides on mild steel in an acidic environment. *Appl. Surf. Sci.* 252, 2139–2152. <https://doi.org/10.1016/j.apsusc.2005.03.178>.
- Pal, A., Das, C., 2022. New eco-friendly anti-corrosion inhibitor of purple rice bran extract for boiler quality steel: Experimental and theoretical investigations. *J. Mol. Struct.* 1251, 131988. <https://doi.org/10.1016/j.molstruc.2021.131988>.
- Pereira, S., Pereira, M., Fernandez, T., Magalhaes, M., Schontag, T., Lago, D., Senna, L., 2012. Inhibitory action of *Aqueous garlic* peel extract on the corrosion of carbon steel in HCl solution. *Corros. Sci.* 65, 360–366. <https://doi.org/10.1016/j.corsci.2012.08.038>.
- Philippe, A., Chahla, R., Mohamed, M., 2020. Corrosion inhibition of copper in 0.5 M NaCl solutions by aqueous and hydrolysis acid extracts of olive leaf. *J. Electroanal. Chem.* 859, 113834. <https://doi.org/10.1016/j.jelechem.2020.113834>.
- Prasad, D., Dagdag, O., Safi, Z., Wazzan, N., Guo, L., 2022. *Cinnamomum tamala* leaves extract highly efficient corrosion bio-inhibitor for low carbon steel: Applying computational and experimental studies. *J. Mol. Liq.* 347, 118218. <https://doi.org/10.1016/j.molliq.2021.118218>.
- Radwan, A.B., Mannah, C.A., Sliem, M.H., Al-Qahtani, N.H.S., Okonkwo, P.C., Berdimurodov, E., Mohamed, A.M., Abdullah, A.M., 2021. Electrospun highly corrosion-resistant polystyrene-nickel oxide superhydrophobic nanocomposite coating. *J. Appl. Electrochem.* 51 (11), 1605–1618. <https://doi.org/10.1007/s10800-021-01603-8>.
- Rani, A., Thomas, A., Arshad, M., Joseph, A., 2022. The influence of aqueous and alcoholic extracts of *Garcinia cambogia* fruit rind in the management of mild steel corrosion in hydrochloric acid: theoretical and electroanalytical studies. *J. Mol. Liq.* 346, 117873. <https://doi.org/10.1016/j.molliq.2021.117873>.
- Rathod, M., Minagalavar, R., Rajappa, S., 2022. Effect of *Artabotrys odoratissimus* extract an environmentally sustainable inhibitor for mild steel corrosion in 0.5 M H₂SO₄ media. *J. Indian Chem. Soc.* 99, 100445. <https://doi.org/10.1016/j.jics.2022.100445>.
- Rezaeivala, M., Karimi, S., Tuzun, B., Sayin, K., 2022. Anti-corrosion behavior of 2-((3-(2-morpholino ethylamino)-N3-(pyridine-2-yl) methyl) propylimino) methyl) pyridine and its reduced form on carbon steel in hydrochloric acid solution: Experimental and theoretical studies. *Thin Solid Films* 741, 139036. <https://doi.org/10.1016/j.tsf.2021.139036>.

- Rodriguez-Perez, C., Gomez-Caravac, A., Guerra-Hernandez, E., Cerretani, L., Garcia-Villanova, B., Verardo, V., 2018. Comprehensive metabolite profiling of *Solanum tuberosum* L. (potato) leaves by HPLC-ESI-QTOF-MS. *Food Res. Int.* 112, 390–399. <https://doi.org/10.1016/j.foodres.2018.06.060>.
- Saini, N., Kumar, R., Lgaz, H., Salghi, R., Chung, I., Kumar, S., Lata, S., 2018. Minified dose of urispas drug as better corrosion constraint for soft steel in sulphuric acid solution. *J. Mol. Liq.* 269, 371–380. <https://doi.org/10.1016/j.molliq.2018.08.070>.
- Salmisfar, A., Edraki, M., Alibakhshi, E., Ramezanzadeh, B., Bahakeh, G., 2021. Theoretical design coupled with experimental study of the effectiveness of the inhibitive molecules based on *Cynara scolymus* L extract toward chloride-induced corrosion of steel. *J. Mol. Liq.* 332, 115742 <https://doi.org/10.1016/j.molliq.2021.115742>.
- Satapathy, A., Gunasekaran, G., Sahoo, S., Amit, K., Rodrigues, P., 2009. Corrosion inhibition by *Justicia gendarussa* plant extract in hydrochloric acid solution. *Corros. Sci.* 51, 2848–2856. <https://doi.org/10.1016/j.corsci.2009.08.016>.
- Shahmoradi, A., Ranjbarghanei, M., Javidparvar, A., Guo, L., Berdimurodov, E., Ramezanzadeh, B., 2021. Theoretical and surface/ electrochemical investigations of *Walnut* fruit green husk extract as effective inhibitor for mild-steel corrosion in 1M HCl electrolyte. *J. Mol. Liq.* 338, 116550 <https://doi.org/10.1016/j.molliq.2021.116550>.
- Sharma, S., Sharmab, Y., 2019. *Cordia dichotoma* as corrosion inhibitor for aluminum alloy (AA6063) in hydrochloric acid. *Port. Electrochim. Act.* 37, 1–22. <https://doi.org/10.4152/pea.201901001>.
- Sigircik, G., Yildirim, D., Tuken, T., 2017. Synthesis and inhibitory effect of N, N'-bis (1-phenylethanol) ethylenediamine against steel corrosion in HCl Media. *Corros. Sci.* 120, 184–193. <https://doi.org/10.1016/j.corsci.2017.03.003>.
- Silva, M., Policarpi, E., Spinelli, A., 2021. *Syzygium cumini* leaf extract as an eco-friendly corrosion inhibitor for carbon steel in acidic medium. *J. Taiwan Inst. Chem. Eng.* 129, 342–349. <https://doi.org/10.1016/j.jtice.2021.09.026>.
- Singh, M.R., Gupta, P., Gupta, K., 2015. The litchi (*Litchi Chinensis*) peels extract as a potential green inhibitor in prevention of corrosion of mild steel in 0.5 M H₂SO₄ solution. *Arab. J. Chem.* 52, 1035–1041. <https://doi.org/10.1016/j.arabj.2015.01.002>.
- Singh, A., Shukla, S., Singh, M., Quraishi, M., 2011. Inhibitive effect of ceftazidime on corrosion of mild steel in hydrochloric acid solution. *Mater. Chem. Phys.* 129, 68–76. <https://doi.org/10.1016/j.matchemphys.2011.03.054>.
- Swaroop, B.S., Victoria, S.N., Manivannan, R., 2016. *Azadirachta indica* leaves extract as inhibitor for microbial corrosion of copper by *Arthrobacter sulfureus* in neutral pH conditions—A remedy to blue green water problem. *J. Taiwan Inst. Chem. Eng.* 64, 269–278. <https://doi.org/10.1016/j.jtice.2016.04.007>.
- Tan, B., Zhang, S., Liu, H., Qiang, Y., Li, W., Lei, G., Chen, S., 2019. Insights into the inhibition mechanism of three 5-phenyltetrazole derivatives for copper corrosion in sulfuric acid medium via experimental and DFT methods. *J. Taiwan Inst. Chem. Eng.* 102, 424–437. <https://doi.org/10.1016/j.jtice.2019.06.005>.
- Tang, M., Li, X., Deng, S., Lei, R., 2021. Synergistic inhibition effect of *Mikania micrantha* extract with KI on steel corrosion in H₂SO₄ solution. *J. Mol. Liq.* 344, 117926 <https://doi.org/10.1016/j.molliq.2021.117926>.
- Tehrani, M., Ghahremani, P., Ramezanzadeh, M., Bahlakeh, G., Ramezanzadeh, B., 2021. Theoretical and experimental assessment of a green corrosion inhibitor extracted from *Malva sylvestris*. *J. Environ. Chem. Eng.* 9, 105256 <https://doi.org/10.1016/j.jece.2021.105256>.
- Thomas, A., Prajila, M., Shainy, K.M., Joseph, A., 2020. A green approach to corrosion inhibition of mild steel in hydrochloric acid using fruit rind extract of *Garcinia indica* (Binda). *J. Mol. Liq.* 312, 113369 <https://doi.org/10.1016/j.molliq.2020.113369>.
- Umoren, S., Obot, I., Israel, A., Asuquo, P., Soloman, M., Eduok, U., Udoh, A., 2014. Inhibition of mild steel corrosion in acidic medium using coconut coir dust extracted from water and methanol as solvents. *J. Ind. Eng. Chem.* 20, 3612–3622. <https://doi.org/10.1016/j.jiec.2013.12.056>.
- Verma, D.K., Kazi, M., Alqahtani, M.S., Syed, R., Berdimurodov, E., Kaya, S., Salim, R., Asatkar, A., Haldhar, R., 2021. N-hydroxybenzothioamide derivatives as green and efficient corrosion inhibitors for mild steel: Experimental, DFT and MC simulation approach. *J. Mol. Struct.* 1241, 130648 <https://doi.org/10.1016/j.molstruc.2021.130648>.
- Vorobyova, V., Skiba, M., Chygyrynets, O., Pylpenko, T., Motronyuk, T., Fateev, Y., 2022. Inhibition efficiency of apricot pomace extract as a “green” corrosion inhibitor. *Mater. Today: Proc.* 50, 456–462. <https://doi.org/10.1016/j.matpr.2021.11.292>.
- Wan, S., Zhang, T., Chen, H., Liao, B., Guo, X., 2022. *Kapok* leaves extract and synergistic iodide as novel effective corrosion inhibitors for Q235 carbon steel in H₂SO₄ medium. *Ind. Crop. Prod.* 178, 114649 <https://doi.org/10.1016/j.indcrop.2022.114649>.
- Wang, J., Ma, X., Tabish, M., Wang, J., 2022. Sunflower-head extract as a sustainable and eco-friendly corrosion inhibitor for carbon steel in hydrochloric acid and sulfuric acid solutions. *J. Mol. Liq.* 367, 120429 <https://doi.org/10.1016/j.molliq.2022.120429>.
- Wang, Q., Tan, B., Bao, H., Xie, Y., Mou, Y., Li, P., Chen, D., 2019. Evaluation of *Ficus tikoua* leaves extract as an eco-friendly corrosion inhibitor for carbon steel in HCl medium. *Bioelectrochemistry* 128, 49–55. <https://doi.org/10.1016/j.bioelechem.2019.03.001>.
- Wang, Q., Zheng, H., Liu, L., Zhang, Q., Wu, X., Yan, Z., Sun, Y., Li, X., 2022. Insight into the anti-corrosion behavior of *Reineckia Carnea* leaves extract as an eco-friendly and high-efficiency corrosion inhibitor. *Ind. Crop Prod.* 188, 115640 <https://doi.org/10.1016/j.indcrop.2022.115640>.
- Wang, Q., Liu, L., Zhang, Q., Wu, X., Zheng, H., Gao, P., Zeng, G., Yan, Z., Sun, Y., Li, Z., Li, X., 2022. Insight into the anti-corrosion performance of *Artemisia argyi* leaves extract as eco-friendly corrosion inhibitor for carbon steel in HCl medium. *Sustain. Chem. Pharm.* 27, 100710 <https://doi.org/10.1016/j.scp.2022.100710>.
- Wazzan, N., 2023. Phytochemical components of *Allium Jesdianum* flower as effective corrosion-resistant materials for Fe(110), Al(111), and Cu(111): DFT study. *Arab. J. Chem.* 16, 104625 <https://doi.org/10.1016/j.arabj.2023.104625>.
- Xu, C., Li, W., Tan, B., Zuo, X., Zhang, S., 2022. Adsorption of *Gardenia jasminoides* fruits extract on the interface of Cu/H₂SO₄ to inhibit Cu corrosion. *Exp. Theor. Stud.* 345, 116996 <https://doi.org/10.1016/j.molliq.2021.116996>.
- Younes, A., El-Maghrabi, H., Ali, H., 2017. Novel polyacrylamide-based solid scale inhibitor. *J. Hazard.* 334, 1–9. <https://doi.org/10.1016/j.jhazmat.2017.03.052>.
- Zaher, A., Aslam, R., Lee, H.S., Khafouri, A., Boufellous, M., Alrashdi, A.A., Elaoufir, Y., Lgaz, H., Ouhssine, M., 2022. A combined computational & electrochemical exploration of the *Ammi visnaga* L. extract as a green corrosion inhibitor for carbon steel in HCl solution. *Arab. J. Chem.* 15, 103573 <https://doi.org/10.1016/j.arabj.2021.103573>.
- Zakaria, F., Hamidon, T., Hussin, M., 2022. Applicability of winged bean extracts as organic corrosion inhibitors for reinforced steel in 0.5 M HCl electrolyte. *J. Indian Chem. Soc.* 99, 100329 <https://doi.org/10.1016/j.jics.2021.100329>.
- Zarrok, H., Zarrouk, A., Hammouti, B., Salghi, R., Jama, C., Bentiss, F., 2012. Corrosion control of carbon steel in phosphoric acid by purpald – Weight loss, electrochemical and XPS studies. *Corros. Sci.* 64, 243–252. <https://doi.org/10.1016/j.corsci.2012.07.018>.
- Zeng, W., Xu, Y., Ge, P., Xiao, W., Liu, Q., Gao, Z., Yan, Y., 2021. *Ipomoea batatas* leaves extract as a green corrosion inhibitor for Q235 steel in HCl solution. *Int. J. Electrochem. Sci.* 16, 211031 <https://doi.org/10.20964/2021.10.40>.
- Zhang, M., Guo, L., Zhu, M., Wang, K., Zhang, R., He, Z., Lin, Y., Leng, S., Anadebe, V., Zheng, X., 2021. *Akebia trifoliata koiaz* peels extract as environmentally benign corrosion inhibitor for mild steel in HCl solutions: Integrated experimental and theoretical investigations. *J. Ind. Eng. Chem.* 101, 227–236. <https://doi.org/10.1016/j.jiec.2021.06.009>.
- Zhang, X., Yang, L., Zhang, Y., Tan, B., Zheng, X., Li, W., 2022. Combined electrochemical/surface and theoretical assessments of *Rosa laevigata* extract as an eco-friendly corrosion inhibitor for copper in acidic medium. *J. Taiwan Inst. Chem. Eng.* 136, 104408 <https://doi.org/10.1016/j.jtice.2022.104408>.
- Zhang, Y., 2007. Study on the biological activity of *sweet potato* stem and leaf extract and its chemical composition. Nanchang, Nanchang University. Doi: 10.1016/d.y1239197.
- Zhu, M., Guo, L., He, Z., Marzouki, R., Zhang, R., Berdimurodov, E., 2021. Insights into the newly synthesized N-doped carbon dots for Q235 steel corrosion retardation in acidizing media: A detailed multidimensional study. *J. Colloid Interf. Sci.* 608, 2039–2049. <https://doi.org/10.1016/j.jcis.2021.10.160>.
- Zuo, X., Li, W., Luo, W., Zhang, X., Qiang, Y., Zhang, J., Li, H., Tan, B., 2021. Research of *Lilium brownii* leaves extract as a commendable and green inhibitor for X70 steel corrosion in hydrochloric acid. *J. Mol. Liq.* 321, 114914 <https://doi.org/10.1016/j.molliq.2020.114914>.